Tunable Surface-enhanced Raman Scattering (SERS) from Nano-aperture Arrays

by

Xiaoqiang Zhang
B.Sc., Beijing Normal University, 2009

A Thesis Submitted in Partial Fulfillment
of the Requirements for the Degree of

MASTER OF SCIENCE

in the Department of Chemistry

Supervisory Committee

Tunable Surface-enhanced Raman Scattering (SERS) from Nano-aperture Arrays

by

Xiaoqiang Zhang
B.Sc., Beijing Normal University, 2009

Supervisory Committee

Dr. Alexandre G. Brolo, (Department of Chemistry)
Supervisor

Dr. David A. Harrington, (Department of Chemistry)
Departmental Member

Dr. Irina Paci, (Department of Chemistry)
Departmental Member

Abstract

Supervisory Committee
Dr. Alexandre G. Brolo, (Department of Chemistry)
Supervisor
Dr. David A. Harrington, (Department of Chemistry)
Departmental Member
Dr. Irina Paci, (Department of Chemistry)
Departmental Member

Research work on fabricating organized and reproducible SERS substrates has been done in this thesis. Nano-aperture arrays with circular, bow-tie and cross bow-tie shapes were fabricated by using FIB milling. These arrays were imaged under SEM and their parameters were measured.

The optical transmission properties of these arrays were measured by white light transmission. It was found that the shape of the nano-aperture could determine these arrays' abilities to support SPR. Different shapes would give different SPR modes and generated optical transmission peaks at varied wavelengths. For nano-aperture array with identical shapes, the varied parameters, such as periodicity or tip-to-tip distances, would affect the position of the transmission peaks. Slight increase or decrease of these parameters can be manipulated to adjust the peak positions, catering to the best resonance of the excitation laser used in Raman spectroscopy.

The enhancement properties of these arrays as SERS substrates were measured by Raman spectroscopy. Different SERS enhancement properties could be found across different shaped nano-aperture arrays and cross bow-tie nano-aperture arrays give the best SERS enhancement. For nano-aperture array with identical shapes, the varied parameters would affect its ability of SERS enhancement. Near field simulations were carried out in order to explain the relationship of the SERS results and these arrays' SPR ability.

Electrochemical study on these ordered nano-aperture arrays was also carried out in this thesis.

Table of Contents

List of Tables

List of Figures

Acknowledgments

A short “*Thanks*” is given here to those helped, though not listed, their work is truly appreciated.

Dedication

to my family members

Chapter 1: Introduction

1.1 Motivation and Objectives

Surface-enhanced Raman scattering (SERS) provides a million fold increase [1-4] in the Raman signal through both charge-transfer resonances [5, 6] and amplification of local electromagnetic fields [7, 8]. The Raman-active molecule must be adsorbed in an appropriated metallic nanostructure to benefit from the SERS effect.

In the 1970s, Fleischman and co-workers [9] discovered this enormous Raman signal enhancement from pyridine adsorbed on an electrochemically roughened silver electrode surface. Future research pointed out that the nano-shaped structures of the rough silver electrode were crucial for the SERS phenomenon, and the large increase in the Raman signal could not be assigned only to an increase in the surface area [6, 10, 11]. Since then, part of the field has focused on the fabrication and optimization of the nanostructures that support the enhancement; the so-called “SERS substrates”. In the late 1990s, the high signal enhancement efficiency observed in SERS allowed researchers to achieve the ultimate limit of single molecule detection [12-15]. The potential for applying this technique to biological molecule characterization [16-19] with high sensitivity drives the pursuit of new types of SERS substrates that provide controllable and reproducible enhancement. In that sense, several works were published in the area of the fabrication of noble metal nanostructures in recent years [20-29]. These efforts focused on the fabrication of structures with improved local electromagnetic field amplification for SERS with various shapes, sizes, and aggregate states.

The huge local electromagnetic field amplification responsible for SERS originates from the excitation of surface plasmon (SP) oscillations [30, 31]. When two metallic nano-particles supporting SPs are close enough to allow coupling, an electromagnetic hot-spot is created between the particles. In the hot spot region, the local electromagnetic field is amplified by one to three orders of magnitude. Molecules at this hot-spot experience the enhanced field, leading to the SERS phenomenon [32]. The size of the “hot-spot” is just a few nano-meters, and the field enhancement drops exponentially with distance from the center of the spot [33-35]. The small size and large spatial variation of the field enhancement in the “hot-spot” leads to challenges related to the preparation of stable and reproducible SERS substrates from nano-particles. For instance, randomly packed nano-particles present a strong spatial variation in “hot-spot” strengths. Moreover, most of the wet chemistry procedures lead to distributions of nano-particle shapes and sizes, resulting in strong batch-to-batch variations in the SERS performance. A general goal in the field is to solve this “reproducibility problem” by fabricating SERS substrates with a stable and a reproducible distribution of hot-spots.

In 2004, our group published some work on the application of ordered circular nano-aperture arrays in SERS [36]. Those arrays of nano-holes on gold films support SPR, which leads to the local electromagnetic field amplification required for SERS. In contrast to the randomly packed nano-particles, the SPR properties of the ordered circular nano-aperture can be controlled by simply changing the periodicity (distance between centers of the holes) of the array. The periodicity is typically in the range of hundreds of nano-meters, which can be easily controlled and reproduced using advanced nano-fabrication techniques, such as focused ion beam (FIB) milling. The stability of the circular nano-aperture arrays showed promises as SERS substrates in terms of reproducibility. However, the SERS enhancement factor observed was lower than observed from random metallic nano-structures. The work described in this thesis focuses on the study of the effects of the shapes of the nano-aperture on the SERS efficiency of the arrays. Bow-tie and cross bow-tie-shaped nano-aperture arrays were fabricated and their properties were characterized and compared to that of the circular nano-aperture array.

Electrochemical SERS studies are generally carried out using roughened electrodes [9]. Electrochemical SERS takes advantage of the potential control to obtain fundamental information relative to the chemical mechanism. The high sensitivity and specificity of SERS allows the study of the chemical reactions in electrochemical conditions. While most work on electrochemical SERS used roughened metal electrodes, this thesis will discuss the effect of the applied electrochemical potential on the SERS from organized nano-aperture arrays. This is one the few examples of electrochemical SERS from organized nano-structures.

1.2 Organization of the Thesis

This thesis is laid out in five chapters, including the introduction (Chapter One).

In Chapter One, the motivation for this type of research is presented, followed by a series of brief backgrounds description of the topics required to the understanding of the main aspects of this work. These topics involve Raman spectroscopy, SERS, nano-aperture arrays, SPR, and statistical analysis.

Chapter Two covers the details of the fabrication of circular, bow-tie, and cross bow-tie nano-aperture arrays. Their specific geometric parameters and tolerances will be described. The experimental setups for both SERS and electrochemical SERS measurements will also be presented, together with details regarding the white light transmission apparatus used to characterize the SPR of the nano-apertures.

Chapter Three is the first of the three result chapters in this thesis. In that chapter, the SPR properties of the circular, bow-tie and cross bow-tie nano-aperture arrays will be presented. The experimental transmission spectra will be compared to calculations using both analytical and numerical (finite-difference time-domain method based) methods. The dependence of the SPR properties on the geometrical parameters of the nano-aperture arrays, such as hole-shape, array periodicity, and tip-to-tip distance in the bow-ties will compared and discussed.

In Chapter Four, SERS results from circular, bow-tie, and cross bow-tie nano-aperture arrays will be given. For each type of aperture array, the dependence of the SERS enhancement on the array periodicity and tip-to-tip distance in the bow-ties will be compared and discussed. The comparison of SERS enhancement properties between different types of nano-aperture arrays will be rationalized. The impact of applied electrochemical potential on the SERS enhancement properties of the nano-aperture array will be presented and discussed. The application of principal components analysis (PCA) method on a time-series SERS signal from circular nano-aperture array was investigated and the result will be discussed.

Chapter Five is a summary of the main finding in this thesis.

1.3 Background

1.3.1 Nano-aperture Arrays

A nano-aperture array is defined in this thesis as a matrix of nano-sized holes punched through a thin metal layer. The holes are distributed in an organized square. The geometric parameters of the structure and the dielectric characteristics of the surrounding environment (air, solution etc.) control the optical properties of the arrays [37].

The concept of using nano-aperture array as SERS substrates is relatively recent compared to the use of nano particles for SERS. The main reason for this is that the main advanced fabrication techniques for the preparation of nano-aperture arrays have just been established in the last twenty years.

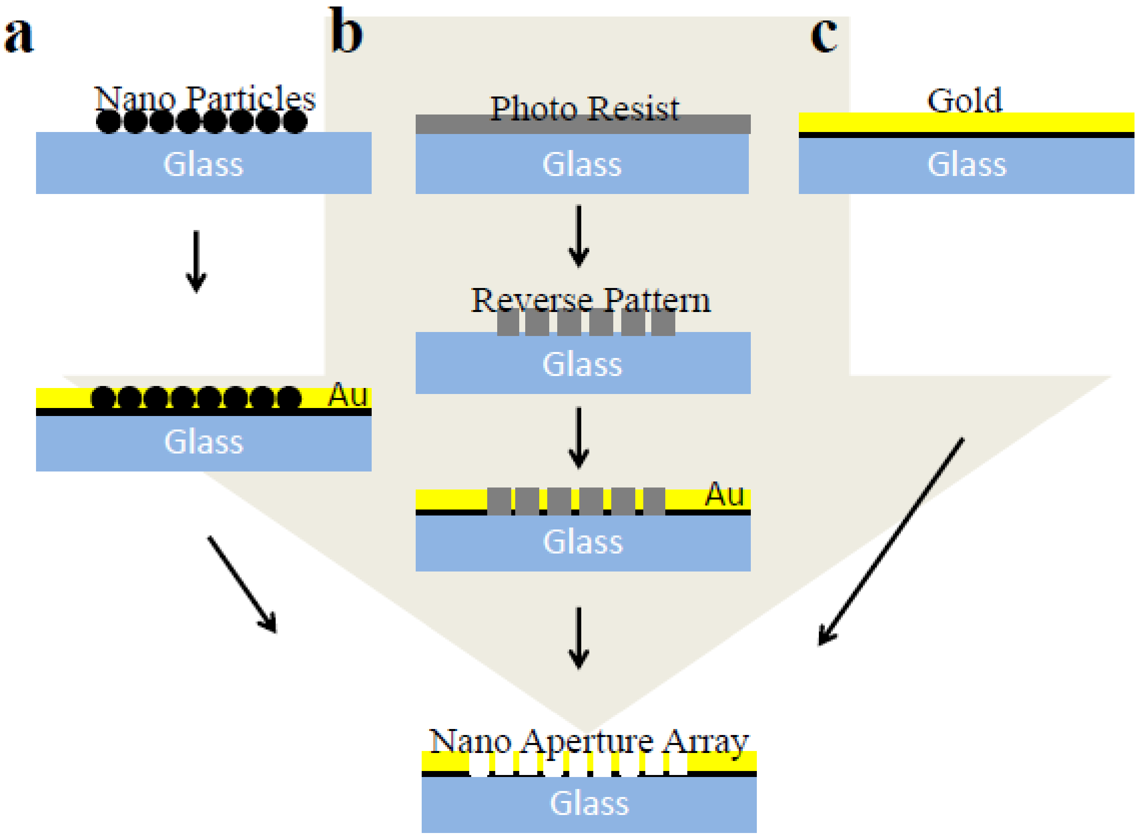

Figure 1.1 Schematic views of micro/nano fabrication procedures to generate nano-aperture arrays: a) and b), deposition method, c) FIB method. The black line between the gold layer and glass layer is the adhesion layer of Cr. In the deposition method, either self-assembly nano-particles or lithography produce photo resist pattern are used to fabricate the periodically arranged metal aperture array. In the FIB method, the periodically arranged metal aperture is fabricated by the designed image.

Two typical fabrication approaches are normally followed to produce nano-aperture arrays.

The first one uses focused ion beam (FIB) milling (see Figure 1.1-c), which is also the fabrication procedure followed in the work presented in this thesis. FIB systems use focused ions (usually gallium) beams to mill away metal atoms (Au, Cr in this work) at designed positions in the metal layer (Figure 1.1c). Various patterns can be designed with common drawing software and then later be adapted by the FIB systems to produce nano-aperture arrays with different geometry, periodicities, and hole-shapes.

In the second approach, nano-aperture fabrication is achieved by depositing the metal in pre-determined patterns. The general principle involves the formation of a reverse pattern to the desired nano-aperture array as a template. Specific metals are then deposited to the reverse template pattern, followed by lift-off to produce the desired nano-aperture array. The shape and periodicity of the nano-aperture arrays are easily controlled by the design of the reverse template patterns.

The reverse template pattern can be generated using different approaches.

For instance, a "bottom up" method involves the self-assembly of nano particles [38, 39] (polystyrene sphere for instance) (see Figure 1.1-a) that interact with each other, forming an ordered monolayer structure on the surface as their solvent slowly evaporates. This ordered structure serves as a template for selected metals that are deposited into the interstice of the packed structure. The nano-aperture array is produced in a final step when the nano-particles are etched away.

E-beam lithography (EBL) [40] (see Figure 1.1-b) can also be used to generate a template for the fabrication of nano-aperture arrays. A layer of polymer (PMMS for instance) is spin-coated onto a glass wafer, and the reverse template pattern is drawn on the polymer with an electron beam, in a process similar to FIB. The focused electron beam is computer controlled to generate the reverse template pattern. After the desired metal is deposited onto this pattern, the template is etched away in an acetone bath to produce the nano-aperture arrays.

Similar to EBL, photo-lithography (see Figure 1.1-b) can also be used to produce nano-aperture arrays. In that case, a photo resist (SU-8 for instance) is spin-coated onto a glass wafer and instead of using electron beam, light is used to generate the reverse template pattern. The reverse pattern is transferred using a mask or simply by using the interference pattern of beams [41]. Selected metals are deposited onto the reverse template and the underlying pattern is removed to produce the nano-aperture array, as described above. However, interference-lithography has the limitation in terms of selecting the hole shape. The interference pattern cannot generate sophisticated shapes, such as the bow-tie shape.

1.3.2 Surface Plasmon Resonance (SPR)

Surface plasmon resonance (SPR) is the result of the excitation of surface plasmons (SPs) waves at the interface between a metal and the surrounding medium [42].

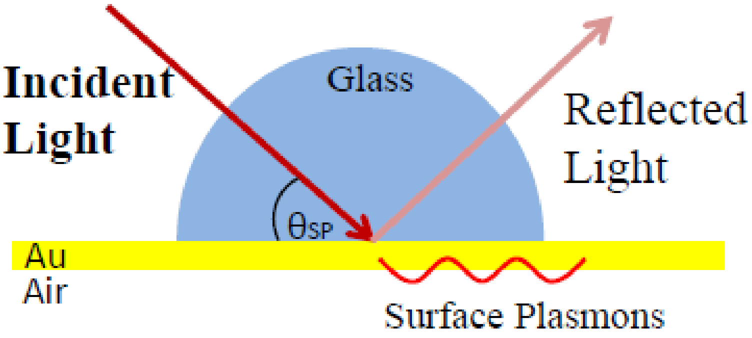

Figure 1.2 Schematic view of surface plasmon resonance: the excitation process of surface plasmons in the Kretschmann configuration.

Figure 1.2 shows a common procedure for SPR generation in the Kretschmann configuration [43]. When the incident monochromatic light reaches a planar gold surface through a glass prism, it will get totally reflected for all incident angles beyond the critical angle. It is called the total internal reflection [44]. However, when an incident angle θ_{SP} is reached, the intensity of the reflected light will drop dramatically. This occurs because part of the energy of the incident light transmitted through the gold layer as the evanescent wave and is used to excite free electrons oscillations at the gold-air interface, SPs [44].

The SPR process can be easily understood as an energy transfer process, in which part of the energy of the incident light gets transferred to the surface plasmons wave. The prerequisite for this energy transfer is the momentum match between the incident light and the SP wave. This momentum match is achieved using the attenuated total reflection (ATR) [45, 46] in prism coupler as demonstrated in the Kretschmann configuration presented in Figure 1.3. It is also possible to excite SP waves using the Otto configuration [47].

Nano-sized metal structures can also be used to sustain SPR.

For instance, Figure 1.3-a shows SPR generation enabled by a diffraction grating [48]. The periodically patterned metal surface will direct the reflected light to different angles (diffraction orders). This process generates a parallel component of the diffracted light with matched momentum that couples to the SP waves at a certain incident angle, θ_{SP}. As the energy of the incident light has been transferred to the SPR, the intensity of the diffracted (reflected) light will drop.

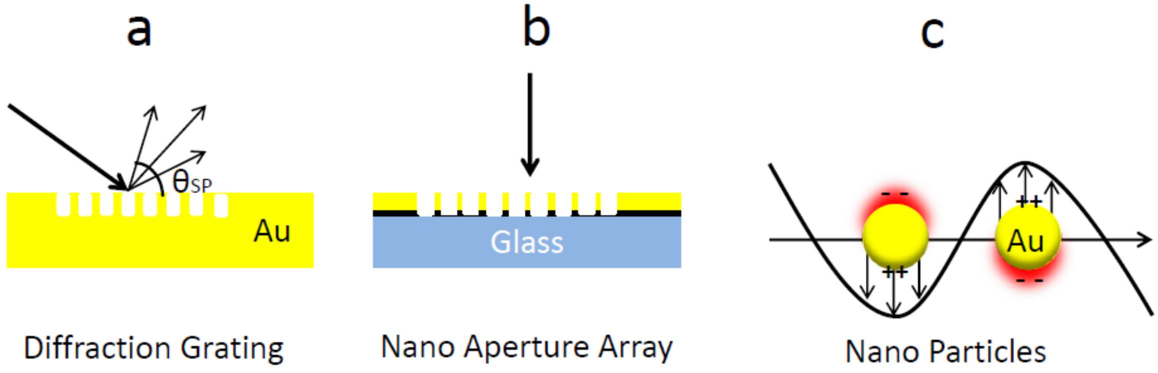

Figure 1.3 Schematic views of nano-sized metal structures for SPR. a) Diffraction grating: the black bold arrow represents the incident light and the other arrows represent the diffracted lights. b) Nano-aperture array: the black arrow represents the incident light. c) Nano particles: black arrows represent the incident light and its electric field.

Figure 1.3-b shows the scheme for a nano-aperture array used for SPR [49]. The incident light is normal to the metal surface and only light with matched wavelengths will be able to excite SP waves for given periodicity. The transmitted light at the SP wavelengths will experience enhanced transmission through the apertures compared to the other wavelengths. This phenomenon is called the extraordinary optical transmission (EOT) [50]. SPR plays an import role in EOT. The periodicity of the nano-aperture array determines which wavelength is enhanced [37]. Thus, when incident white light reaches the nano-aperture array at normal incidences, only a few wavelengths are transmitted efficiently. White light transmission spectroscopy [49] can be used to characterize the SPR properties of different nano-aperture array. In that case, a transmission maximum is observed for each wavelength that satisfied the SPR properties of the nano-structure.

Figure 1.3-c shows that localized SPR can also be excited in nano-sized metal particles. The free classical electrons in the nano-particles (represented by the red cloud) will be modulated by the external electromagnetic force. Then, the electrostatic force of the separated charges will drag the electrons back. Since the electromagnetic force has a sinusoidal form, the free electrons will oscillate around the metal particle to generate a dipolar SPR response [30].

The common feature of the Kretschmann configuration (Figure 1.2), the diffraction grating (Figure 1.3-a), and the nano-aperture arrays (Figure 1.3-b) is that all these arrangements allow the momenta between the incident light and the SP to be matched.

all based on the fact that they can match the momentums between the incident light and the SP.

$$\left|\overrightarrow{k_{SP}}\right| = \left|\overrightarrow{k_{\lambda}}\right|\left(\frac{\epsilon_{eff}\epsilon_m}{\epsilon_{eff}+\epsilon_m}\right)^{1/2} \tag{1.1}$$

Equation 1.1 shows the relationship between the SP's momentum $\left|\overrightarrow{k_{SP}}\right|$ and the incident light's momentum $\left|\overrightarrow{k_{\lambda}}\right|$. ϵ_{eff} is the effective permittivity at the metal-dielectric interface, and ϵ_m is the real part of the permittivity of the metal. Under normal situations, the value of $\left(\frac{\epsilon_{eff}\epsilon_m}{\epsilon_{eff}+\epsilon_m}\right)^{1/2}$ is always bigger than 1. Therefore, extra momentum is required to match $\left|\overrightarrow{k_{\lambda}}\right|$ and $\left|\overrightarrow{k_{SP}}\right|$.

For the situation of diffraction grating, including nano-aperture arrays, the extra momentum is given by:

$$\vec{G} = \pm\left(i\frac{2\pi}{p}\right)\vec{x} \pm \left(j\frac{2\pi}{p}\right)\vec{y} \tag{1.2}$$

Whose value is:

$$\left|\vec{G}\right| = \frac{2\pi}{p}\left(\sqrt{i^2+j^2}\right) \tag{1.3}$$

Equation 1.2 shows the extra momentum due to a squre nano-aperture array. *i* and *j* are integers; p is the periodicity of the nano-aperture array and $\vec{x}$ and $\vec{y}$ show the unit vectors. The match between the SP momentum and the incident light momentum is reached when:

$$\left|\overrightarrow{k_{SP}}\right| = \left|\overrightarrow{k_{\lambda||}}\right| + \left|\vec{G}\right| \tag{1.4}$$

Equation 1.4 can be rewritten as the following when Equation 1.1 is considered.

$$\left|\overrightarrow{k_\lambda}\right|\left(\frac{\epsilon_{eff}\epsilon_m}{\epsilon_{eff}+\epsilon_m}\right)^{1/2}=\left|\overrightarrow{k_{\lambda||}}\right|+\left|\vec{G}\right| \tag{1.5}$$

In Equation 1.5, the value of $\left|\overrightarrow{k_{\lambda||}}\right|$ is zero because the incident light is normal to the nano-aperture array surface, therefore:

$$\left|\overrightarrow{k_\lambda}\right|\left(\frac{\epsilon_{eff}\epsilon_m}{\epsilon_{eff}+\epsilon_m}\right)^{1/2}=\left|\vec{G}\right|=\frac{2\pi}{p}\left(\sqrt{i^2+j^2}\right) \tag{1.6}$$

Since $\left|\overrightarrow{k_\lambda}\right|=\frac{2\pi}{\lambda}$ and the wavelength $\boldsymbol{\lambda}$ of the incident light is the same of the excited SP wavelength λ_{SP}. Equation 1.6 can be written as:

$$\frac{2\pi}{\lambda_{SP}}\left(\frac{\epsilon_{eff}\epsilon_m}{\epsilon_{eff}+\epsilon_m}\right)^{1/2}=\frac{2\pi}{p}\left(\sqrt{i^2+j^2}\right) \tag{1.7}$$

Equation 1.7 is also the equation to calculate the wavelength of the excited SP for the square array of circular nano-aperture:

$$\lambda^{SP}(i,j)=p(i^2+j^2)^{-1/2}\left(\frac{\epsilon_{eff}\epsilon_m}{\epsilon_{eff}+\epsilon_m}\right)^{1/2} \tag{1.8}$$

1.3.3 Surface-enhanced Raman Scattering (SERS)

SERS is an increase in the intensity of Raman scattering for molecules adsorbed on nano-structured metals. This process involves both local field amplifications and charge-transfer resonances, which are related to the electromagnetic (EM) and the chemical or charge transfer mechanisms respectively. For an understanding of SERS, basic Raman scattering concepts is introduced below, together with a general description of the EM and the chemical mechanisms.

1.3.3.1 Raman Scattering

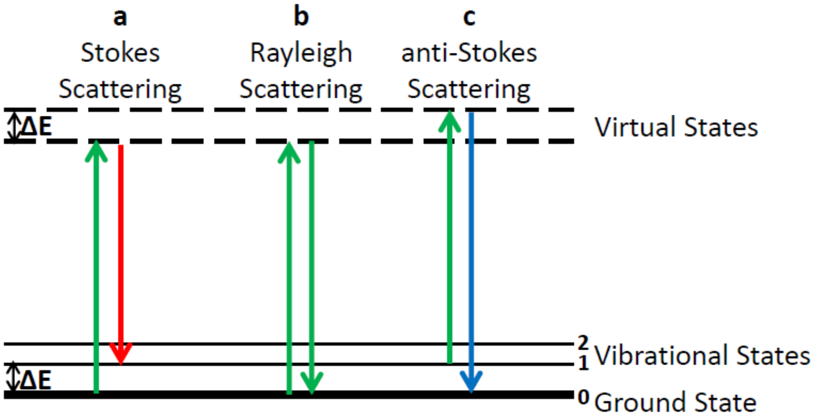

Figure 1.4 Schematic view of the Jablonski diagram showing: a), Stokes scattering, b), Rayleigh scattering, c), anti-Stokes scattering.

Molecule can scatter light elastically or in-elastically. Elastic scattering does not involve energy transfer between the incident and the scattered fields. This is called Rayleigh scattering. Inelastic scattering is relatively rare and involves energy transfer between the molecule and the incident photon. There are two sub-types of inelastic scattering: The Stokes scattering, which results in photons with less energy than the incident photons; and the anti-Stokes scattering: which results in photons with higher energy than the incident photons. Together, the Stokes and anti-Stokes scattering are called Raman scattering in honour of C.V. Raman who first observed the effect [51].

Figure 1.4 shows the simplified Jablonski diagrams, which provide a relative comprehensive way to represent the three different types of light scattering by molecules [52]. The molecular energy states are represented by black lines.

Incident light excites a molecule to a virtual state (an imaginary state represented by the dotted line in Figure 1.4). Molecules at the virtual states do not stay there very long and they normally fall back to the same initial electronic and vibrational state. The photon emitted during the relaxation process has the same energy as the incident photon, characterizing the Rayleigh scattering. On the other hand, if the molecule relaxes to the first excited vibrational state in the electronic ground state, the scattered photon has lower energy than the incident photon, and this is the Stokes scattering. In the anti-Stokes scattering, the energy of the incident light is lower than the scattered light, as shown in Figure 1.4.

In both types of scattering, Stokes and anti-Stokes, there is an energy difference between the incident and the scattered light. This energy difference is called Raman shift, and it is plotted in the horizontal axis of a Raman spectrum in wave number (cm^{-1}).

Figure 1.4 also shows that molecules must be vibrationally excited to generate anti-Stokes scattering. This explains why the anti-Stokes scattering occurrence probability is always lower than the Stokes scattering. The population of the first vibrational state is given by the Boltzmann distribution and, therefore, it is temperature dependent.

An increase of 3 to 5 orders of magnitudes in Raman intensity is observed when the incident light wavelength is near the analyte molecule’s absorption peak. Under this situation, electrons in the scattering process would be excited to a real electronic state instead of a virtual state. This phenomenon is called the resonance Raman scattering [53].

1.3.3.2 Classical Formalism for the Raman Scattering [54]

Raman scattering can be simply understood as the process where light interacts with a molecule and scatters with a different energy. Some understanding of the nature of both light and molecule are required to explain this process.

Light is simply modeled as a single frequency electromagnetic wave with sinusoidal variations of the electric and magnetic fields in both time and space. Only the electric field component is required to discuss the Raman effect.

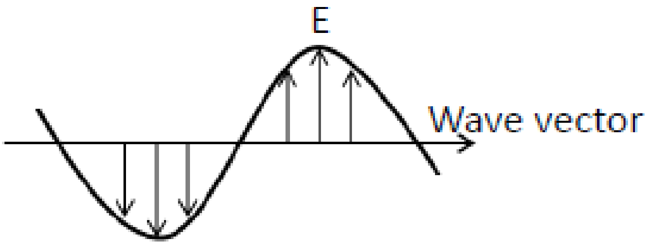

Figure 1.5 Schematic view of the sinusoidal electric field variation of the light.

Figure 1.5 shows the schematic representation of the sinusoidal variation of the electric field of the light with time. The electric field intensity *E* at one point is a part of the maximum electric field amplitude E_0. *v* is the frequency of the light, *t* is the time. *E* is then represented by Equation 1.1:

$$E = E_0 \cos(2\pi v t) \qquad (1.9)$$

Molecule is simply modeled as a positively charged core (nuclei) immersed in negatively charged electron cloud. The nuclei and electron cloud are attracted to each other by electrostatic forces.

Figure 1.6 Schematic view of a) the nuclei/electron cloud model for molecule (HCl for instance), and b) the situation when it is under external electric field *E* and the induced

dipole moment P. The black dots represent the nuclei, and the yellow part represents the electron cloud.

As shown in Figure 1.6, when a molecule is placed under the electric field from the incident light, a displacement of the electron cloud relative to the positive center (core, nuclei) occurs. This displacement would induce a charge separation and a dipole moment P given by Equation 1.10.

$$P = \alpha E \tag{1.10}$$

α is called the polarizability and it is a function of the vibrational normal coordinate q.

For a molecule with N atoms, there are 3N-6 vibrational modes (3N-5 if the molecule is linear). Therefore, there are 3N-6 (3N-5 if linear) vibrational normal coordinates q. The relationship between the polarizability α and each normal coordinate for a vibrational mode i, q_i (i=3N-6, or 3N-5 if linear), is represented by the following function.

$$\alpha = F\left(q_{1,}q_{2,}\dots q_i\right) \tag{1.11}$$

This function can be expanded into a Taylor series.

$$\alpha = \alpha_0 + \sum_{i=1}^{3N-6}\left(\frac{\partial\alpha}{\partial q_i}\right)_0 q_i + \frac{1}{2}\sum_{i=1,j=1}^{3N-6}\left(\frac{\partial^2\alpha}{\partial q_i q_j}\right)_0 q_i q_j + \cdots \tag{1.12}$$

Equation 1.12 shows that the polarizability α of a specific molecule is the combination of many α due to each vibrational mode. Because the first two components are much more important compared to the rest, the polarizability α could be simplified as the following Equation 1.13.

$$\alpha = \alpha_0 + \sum_{i=1}^{3N-6}\left(\frac{\partial\alpha}{\partial q_i}\right)_0 q_i \tag{1.13}$$

Each molecule vibrational mode has its own frequency ν_m. Thus, the normal coordinate q_i can be written as:

$$q_i = q_0 \cos(2\pi\nu_m t) \tag{1.14}$$

The combination of Equation 1.13 and Equation 1.14 yields an expression for the polarizability α as function of the molecular vibration frequency ν_m. For the reason of simplicity, one mode has been picked out for the rest of this demonstration.

$$\alpha = \alpha_0 + \left(\frac{\partial\alpha}{\partial q_i}\right)_0 q_0 \cos(2\pi\nu_m t) \tag{1.15}$$

The combination of Equation 1.9, Equation 1.10 and Equation 1.15 will make the induced dipole moment, P, a function related to the frequency of the incident light, ν, and the molecular vibrational frequency, ν_m.

$$P = \alpha E = [\alpha_0 + (\frac{\partial \alpha}{\partial q_i})_0 q_0 \cos(2\pi \nu_m t)] \times [E_0 \cos(2\pi v t)] \quad (1.16)$$

The trigonometric identity in the following equation is applied to Equation 1.16.

$$\cos A \times \cos B = \frac{1}{2}[\cos(A + B) + \cos(A - B)] \quad (1.17)$$

Equation 1.16 after the application of Equation 1.17 yields the following:

$$P = \alpha_0 \times E_0 \cos(2\pi v t) + (\frac{\partial \alpha}{\partial q_i})_0 q_0 E_0 [\cos(2\pi v t) \cos(2\pi \nu_m t)] \quad (1.18)$$

$$P = \alpha_0 \times E_0 \cos(2\pi t) v + \frac{1}{2}\left(\frac{\partial \alpha}{\partial q_i}\right)_0 q_0 E_0 [\cos\big(2\pi t(v + \nu_m)\big) + \cos\big(2\pi t(v - \nu_m)\big)] \quad (1.19)$$

Equation 1.19 is composed of three parts related directly to three different frequencies, v, $\nu + \nu_m$, and $\nu - \nu_m$. The oscillating dipole will radiate light with these frequencies that correspond to the three scattering situations described in Figure 1.12. The radiated light with the frequency ν shares the same frequency as the incident light. This corresponds to the Rayleigh scattering. The radiated light with the frequency $\nu - \nu_m$ has a frequency lower than the incident light (thus higher wavelength), corresponding to the Stokes scattering. The radiated light with the frequency $\nu + \nu_m$ has a frequency higher than the incident light (thus lower wavelength) and corresponds to the anti-Stokes scattering.

Equation 1.19 also shows that $\left(\frac{\partial \alpha}{\partial q_i}\right)_0$ needs to be non-zero for a molecule to be Raman active. This means that the polarizability α needs to change when the vibrational coordinate q_i changes.

1.3.3.3 The Electromagnetic (EM) Mechanism of SERS

Noble metal particles, with diameter (normally 10 nm to 100 nm) smaller than the wavelength of the incident light, are normally used as a model for the explanation of the EM mechanism in SERS. As illustrated in Figure 1.3-c, this kind of metal structure is able to support SPR. The interaction between the SPR and the light fields (the incident light and the scattered light) acts as one of the main mechanisms in SERS signal amplification phenomenon. This is called the EM mechanism of SERS [55].

The relationship between the light intensity, I, and the light's electromagnetic field E can be represented by the following equation:

$$I = \frac{c\varepsilon_0 n}{2}|E|^2 \tag{1.20}$$

In which, c is the speed of light, ε_0 is the vacuum permittivity, and n is the reflective index.

In the EM theory of SERS, the local field (small area where the analyte molecule is located) is increased. The SERS signal experiences two different enhancement, the enhancement of the local filed at the excitation energy ($E_{(\omega 0)}$) and the enhancement of the local field at the energy of the emitted Raman photon ($E_{(\omega R)}$). Therefore the total enhancement is proportional to the product $|E(\omega_0)|^2\ |E(\omega_R)|^2$. Since the energy of the Raman-shifted photon is normally similar to the excitation energy ($\omega_{0\ \approx}\ \omega_R$); the enhancement can be approximately calculated by using only the local excitation field. Therefore, an enhancement factor G quantifies the increase in the Raman signal and it is defined as considering the Equation 1.20:

$$G = \left|\frac{E_{local}}{E_{incident}}\right|^4 \tag{1.21}$$

The magnitude of the local field can be evaluated analytically for a single molecule absorbed on a single metal particle [56]. In this simplified model, the EM enhancement factor G is represented by the following relation:

$$G \propto \frac{\varepsilon_{1(w)} - \varepsilon_{2(w)}}{\varepsilon_{1(w)} + 2\varepsilon_{2(w)}} \tag{1.22}$$

In which, $\varepsilon_{1(w)}$ is the complex optical dielectric function of the metal. $\varepsilon_{2(w)}$ is the optical dielectric function of the metal particle's environment. w shows that the values of $\varepsilon_{1(w)}$ and $\varepsilon_{1(w)}$ are related to the incident frequency.

It can be found that the intensity of the Raman signal is related to the both the incident light's electric field and the local field's magnitudes from Equation 1.20 and Equation 1.21. Under SPR condition, the ability of a SERS substrate of amplifying the local field plays an important role in the signal intensity. Equation 1.22 shows that this amplifying ability of the SERS substrates is dependent on the optical properties of both the metal and the environment, under the classical approximation of a single nano-particle as substrate.

1.3.3.4 The Chemical Mechanism of SERS

Raman scattering process involves the excitation of a molecule to a virtual state followed by relaxation. Resonance Raman scattering occurs when the excitation energy matches a real electronic state and it leads to a 3 to 5 orders of magnitude increase in the Raman signal intensity. A similar effect might be observed in SERS when the Fermi level of the metal falls near the energy levels of the adsorbed molecule. In that case, excitation with the appropriated laser energy can promote a metal to adsorbate charge transfer transition that would increase the Raman cross-section. This phenomenon is similar to the resonance Raman mechanism and provides an additional contribution to the overall enhancement in SERS. This contribution is called “chemical” or “charge transfer” mechanism [57]. The role of the chemical mechanism can be confirmed by the observation of enhanced Raman signal from surfaces of materials that do not support surface plasmon excitation [58].

1.3.4 SERS Substrates

As discussed above, the ability to support SPR is an important condition for a metal structure to produce SERS. These will be illustrated in this section, where three commonly used structures that support SERS (SERS substrates) will be discussed.

1.3.4.1 Metallic Nano Particles

Metallic nano particles are the most used substrate in SERS [59]. The first type of SERS substrate was an electrochemically roughened Ag electrode, which can be viewed as aggregated Ag nano particles produced by electrochemical redox cycles [9]. During a redox cycle, Ag atoms from the surface of the electrode get oxidized into the solution and they are soon reduced to the neutral atom form when the potential sweep direction is reversed. Instead of returning to their original position, these Ag atoms form nano particles aggregates on the electrode.

Metallic nano particles produced from wet chemistry provides an easy method to fabricate SERS substrates [59]. There are several advantages of producing metallic nano particles for SERS through wet chemistry. First, nano particles can be added to any analyte without requiring an electrochemical setup. Second, the synthesis parameters can be controlled to lead to nano particles with desired sizes and shapes and with SPR properties optimized for the excitation condition of a particular experiment [60].

1.3.4.2 Thin Metal Films

As discussed in Section 1.3.2, SPR in a smooth metal surface cannot be directly generated by direct excitation. One commonly used method to generate SPR is the prism-coupling (Kretschmann configuration) excitation scheme [61].

The prism enables the momentum match between the incident light and the SP waves (see Section 1.3.2). Analyte molecules attached to the Au-Air interface will experience the enhanced electric field, leading to SERS. The Raman signal is only enhanced when the incident angle matches the angle for SPR (θ_{SP}). This shows straightforwardly the relationship between SPR and SERS [62]

1.3.4.3 Nano-aperture Array

As shown in Figure 1.3-b, periodically arranged nano apertures in metal films support SPR. The periodicity of the nano-aperture array needs to be adjusted to tune SPR to the appropriated wavelength. The SPR couples with the incident field, amplifying the local electric field to enable SERS [36].

Another advantage of the nano-aperture arrays based SERS is that it can be used as working electrodes and thus be adapted to study electrochemical process by SERS, as presented in Chapter 4.

1.3.5 The SPR Characterization: Absorption, Extinction, and EOT

The ability of SPR to amplify local fields is the main concerns of this work. Since SERS and SPR are correlated, the enhancement properties of a SERS substrate can be characterized by evaluating its SPR characteristics.

The extinction spectrum can be used to characterize the SPR properties of nano particles colloidal suspensions. These are obtained using regular UV-Vis spectroscopic setups. The position and the intensity of the SPR extinction peak in the SPR spectrum depends on the nano particles size, shape, and aggregation state [60].

In the Kretschmann configuration based SERS, Raman scattering is maximum at $\theta_{SP,}$ which corresponds the minimum in the reflectance [61]. The position of the angle θ_{SP} is wavelength dependent.

Light transmitted through nano-aperture arrays in metal films can excite SPR when the appropriate momentum matching conditions are achieved (Section 1.3.2) [49]. Parameters of the nano-aperture arrays, such as their periodicities, or relative to the shape of the aperture, the tip-to-tip distance in bow-tie shaped apertures, for instance, can be independently tuned to generate SPR at the desired wavelength [49]. Extra Ordinary Transmission (EOT) is observed at the SPR wavelengths (Section 1.3.2), which can be readily determined by measuring the white light transmission at a fixed angle. Several transmission maxima (SPR peak) are observed in the transmitted spectrum, each one of them is related to a particular SPR mode from the nano-aperture array.

Although it is well acknowledged that SPR plays an important role in SERS, the excitation wavelength that leads to optimum SERS from a particular substrate does not always coincide with the SPR peak for the substrate [63]. This is because SERS depends mainly on the intensity of the local field, and there might be stronger at wavelengths that are different than the SPR peak [63]. For example, the “hot spots” (region of high local field intensity) in metallic nano particles aggregated show a complex spatial distribution of intensities [64]. The calculation of the local field strength by numerical methods is then an important tool to complement the SPR characterization of the substrate by optical spectroscopy [65, 66].

1.3.6 Effect of Applied Electrochemical Potential

The application of external electrochemical potential to SERS substrates may result in several different kinds of impact. For instance, the external potential can tune the position of the Fermi level of the metallic substrates, leading to a modulation of the SERS signal through the chemical (charge transfer) mechanism (Section 1.3.3.4) [5, 6]. The potential also controls the surface charge an influences the electrostatic interaction between the substrate and a charged analyte.

As discussed in Section 1.3.3.1, the normal Raman is enhanced when the excitation wavelength matches an internal molecular transition (resonance Raman effect). Similarly, a resonance-Raman like mechanism is operative in SERS when the incident laser energy matches a charge transfer transition between the metal and the adsorbate. The applied electrochemical potential can either increase or decrease the position of the Fermi level of the metallic substrate, allowing a match with the charge transfer transition to be observed at a particular potential. As a result, an optimum in the SERS intensity is generally observed in electrochemical SERS at particular potential [67].

Common analyte molecules used in SERS, such as Rhodamine 6G, congo red, Oxazine 720, and Nile blue, are ionic in aqueous solutions. The relative amount of these molecular ions in solution compared to the adsorbed to the surface is given by the adsorption equilibrium. The applied electrochemical potential changes the surface charges and the electrostatic characteristics of the surface, affecting the equilibrium condition. SERS requires the analyte molecule to be located at the area with enhanced local field (hot spot). The increase in the number of the analyte molecules at hot spot areas lead to a higher SERS intensity. Therefore, the applied electrochemical potential would affect the SERS signal by changing the number of analyte molecules at the hot spot [68].

1.3.7 Rhodamine 6G

Rhodamine 6G (R6G) is a laser dye that is generally used as molecular probe in SERS studies due to its high Raman cross section. The Rhodamine 6G molecule contains a xanthene and a carboxyphenyl groups (see Figure 1.7). These two major π systems act as the chromophores responsible for the R6G strong absorption in aqueous solution at 530 nm with a vibronic shoulder around 470 nm [1] (see Figure 1.8).

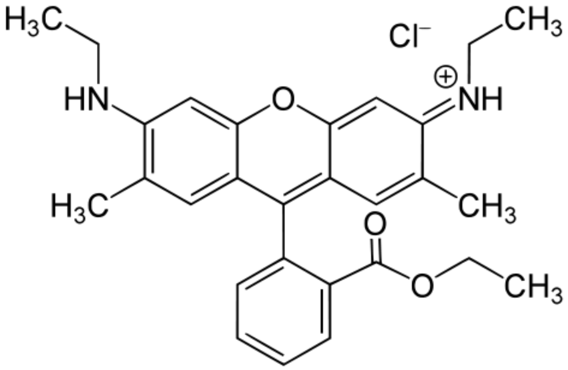

Figure 1.7 Molecular structure of Rhodamine 6G.

Although aqueous solutions of R6G presents fluorescence at 550 nm (see Figure 1.9) when excited by blue/green radiation (450 nm to 570 nm), the emission is quenched when R6G is adsorbed on metallic surfaces, as is the SERS case [1]. This eliminates the emission background and isolates the vibrational bands of the probe molecule. The large Raman cross section of R6G is significantly enhanced in SERS studies [12-15]. R6G is a cationic dye and its adsorption properties can be easily manipulated by the applied electrochemical potentials [68].

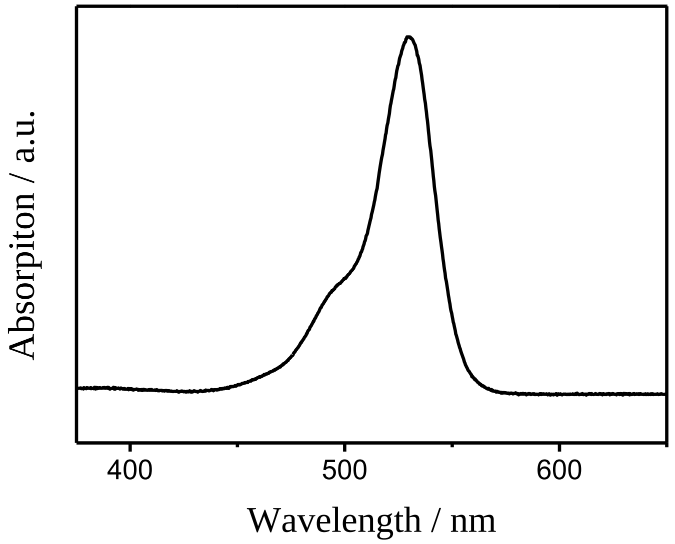

Figure 1.8 Absorption spectrum of Rhodamine 6G. A strong peak at 530 nm with a vibronic shoulder around 470 nm could be observed.

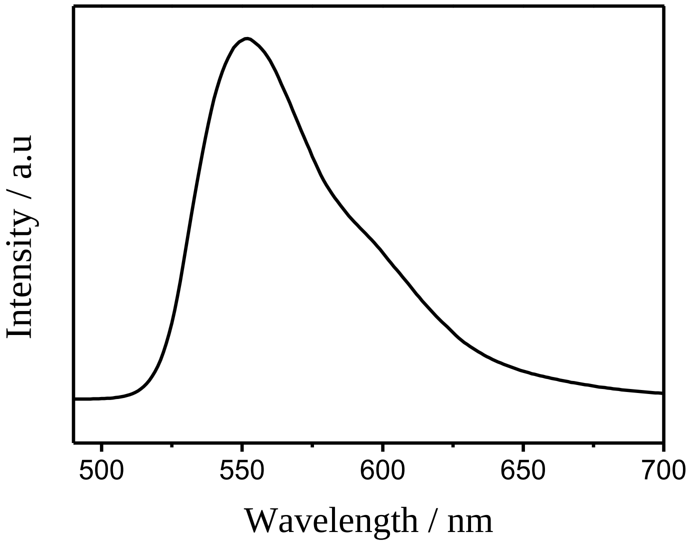

Figure 1.9 Fluorescence emission spectrum of Rhodamine 6G. A strong fluorescence band from 520 nm to 640 nm could be observed.

This thesis will focus on the Raman scattering of R6G in the Raman shift range between of 1000 cm^{-1} to 1700 cm^{-1}. The typical R6G vibrational bands in this range and their assignment are shown in Table 1.1.

Table 1.1 Assignment of selected vibrational bands for Rhodamine 6G [1, 69].

NRS	RRS	SERS	Calculation	Assignment
1184	1178, 1187	1181, 1183	1185	C-H ip bend, ip XRD, C-H bend, N-H bend
1312	1310, 1312	1310	1297	ip XRB N-H bend, CH_2 wag
1364	1361, 1365	1363	1346	XRS, ip C-H bend
1512	1505, 1509	1509	1497	XRS, C-N str, C-H bend, N-H bend
1577	1575, 1577	1572, 1575	1551	arom C-C str, XRS, ip N-H bend
1651	1649, 1652	1650	1643	arom C-C str, XRS, ip C-H bend

NRS_normal Raman scattering; RRS_resonance Raman scattering; All the vibrational frequencies are in the unit of cm^{-1}. Ip_in-plane; XRD_ xanthene ring deformations; XRS_xanthene ring stretch; XRB_xanthene ring breathing.

1.3.8 Principal Components Analysis (PCA)

Principal component analysis (PCA) provides a method to increase signal-to-noise ratio and to filter out spectra due to sample degradation from a large data set [68].

A Raman spectrum data is represented by the signal counts per seconds at a given Raman shift. Therefore, each Raman spectrum is a 2×N matrix, composing of one Raman shift column and one Raman intensity column. Thousands of spectra, obtained in a time series, for instance results in thousands intensity matrixes. Because these intensity data represents the signal for the same sample, they can be combined to form an M×N matrix (M means the number of spectra). The principal component analyse of this M×N matrix can be carried out using a statistical program language called R.

After the treatment from the R program, the Raman intensity data is re-presented by only the first two principal components. This procedure allows each spectrum to be re-plotted with decreased noise level. It also helps differentiate spectra with abnormal peaks, which result mostly from photo degradation of the sample.

Reference:

[1] Hildebrandt P, Stockburger M **1984** Surface-Enhanced Resonance Raman Spectroscopy of Rhodamine 6G Adsorbed on Colloidal Silver *J. Phys. Chem.* 88, 5935-5944

[2] Pettinger B, Krischer K **1987** Comparison of Cross-Sections for Absorption and Surface-enhanced Resonance Raman Scattering for Rhodamine 6G at Coagulated Silver Colloids *J. Electron Spectrosc. Relat. Phenom.* 45, 133-142

[3] Kneipp K **1988** High-Sensitive SERS on Colloidal Silver Particles in Aqueous Solution *Exp. Tech. Phys. (Berlin)* 36, 161-166

[4] Kneipp K, Wang Y, Dasari RR, Feld MS **1995** Approach to Single Molecule Detection Using Surface-Enhanced Resonance Raman Scattering (SERRS): A Study Using Rhodamine 6G on Colloidal Silver *Appl. Spectrosc.* 49, 780-784

[5] Cardona M, Guntherodt G **1984** Light Scattering in Solids IV: Electronic Scattering, Spin Effects, SERS and Morphic Effects *Springer-Verlag: Berlin, Germany* 1984, 289-418

[6] Persson BN **1981** on the Theory of Surface-enhanced Raman Scattering *Chem. Phys. Lett.* 82, 561-565

[7] Creighton JA, Blatchford CG, Albrecht MG **1979** Plasma Resonance Enhancement of Raman-Scattering by Pyridine Adsorbed on Silver or Gold Sol Particles of Size Comparable to the Excitation Wavelength. *J. Chem. Soc., Faraday Trans II* 75, 790-798

[8] Moskovits M **1978** Surface Roughness and the Enhanced Intensity of Raman Scattering by Molecules Adsorbed on Metals *J. Chem. Phys.* 69, 1459-1461

[9] Fleischman M, Hendra PJ, McQuillan AJ **1974** Raman-Spectra of Pyridine Adsorbed at a Silver Electrode *Chem. Phys. Lett.* 26, 163-166

[10] Jeanmaire DL, Van Duyne RP **1977** Surface Raman Spectroelectrochemistry: Part I. Heterocyclic, Aromatic, and Aliphatic-Amines Adsorbed on Anodized Silver Electrode *J. Electroanal. Chem.* 84, 1-20

[11] Albrecht MG, Creighton JA **1977** Anomalously Intense Raman Spectra of Pyridine at a Silver Electrode *J. Am. Chem. Soc.* 99, 5215–5217

[12] Nie S, Emory SR **1997** Probing Single Molecules and Single Nanoparticles by Surface-Enhanced Raman Scattering *Science* 275, 1102-1106

[13] Kneipp K, Wang Y, Kneipp H, Perelman LT, Itzkan I, Dasari RR, Feld MS **1997** Single Molecule Detection Using Surface-Enhanced Raman Scattering (SERS) *Phys. Rev. Lett.* 78, 1667-1670

[14] Kneipp K, Kneipp, H, Deinum G, Itzkan I, Dasari RR, Feld MS **1998** Single-Molecule Detection of a Cyanine Dye in Silver Colloidal Solution Using Near-Infrared Surface-Enhanced Raman Scattering *Appl. Spectrosc.*52, 175-178

[15] Kneipp K, Kneipp H, Kartha B, Manoharan R, Deinum G, Itzkan I, Dasari RR, Feld MS **1998** Detection and Identification of a Single DNA Base Molecule using Surface-enhanced Raman Scattering (SERS) *Phys. Rev. E.*57, R6281-R6284

[16] Suh JS, Moskovits M **1986** Surface-Enhanced Raman Spectroscopy of Amino Acids and

Nucleotide Bases Adsorbed on Silver *J. Am. Chem. Soc.* 108, 4711-4718

[17] Gu HY, Yu AM, Chen HY **2001** Direct Electron Transfer and Characterization of Hemoglobin Immobilized on a Au Colloid–Cysteamine-Modified Gold Electrode *J. Electro. Chem*. 516, 119-126

[18] Grubisha DS, Lipert RJ, Park HY, Driskell J, Porter MD **2003** Femtomolar Detection of Prostate-Specific Antigen: An Immunoassay Based on Surface-Enhanced Raman Scattering and Immunogold Labels *Anal. Chem.* 75, 5936-5943

[19] Cao YC, Jin R, Nam JM, Thaxton CS, Mirkin CA **2003** Raman Dye-Labeled Nanoparticle Probes for Proteins *J. Am. Chem. Soc.* 125, 14676-14677

[20] Doering WE, Nie S **2002** Single-Molecule and Single-Nanoparticle SERS: Examining the Roles of Surface Active Sites and Chemical Enhancement *J. Phys. Chem. B* 106, 311-317

[21] Xiong Y, McLellan JM, Chen J, Yin Y, Li ZY, Xia Y **2005** Kinetically Controlled Synthesis of Triangular and Hexagonal Nanoplates of Palladium and Their SPR/SERS Properties *J. Am. Chem. Soc.*127, 17118-17127

[22] Krug JT II, Wang GD, Emory SR, Nie S **1999** Efficient Raman Enhancement and Intermittent Light Emission Observed in Single Gold Nanocrystals *J. Am. Chem. Soc.* 121, 9208-9214

[23] Camden JP, Dieringer JA, Wang Y, Masiello DJ, Marks LD, Schatz GC, Van Duyne RP **2008** Probing the Structure of Single-Molecule Surface-Enhanced Raman Scattering Hot Spots *J. Am. Chem. Soc.* 130, 12616-12617

[24] Jiang J, Bosnick K, Maillard M, Brus L **2003** Single Molecule Raman Spectroscopy at the Junctions of Large Ag Nanocrystals *J. Phys. Chem. B* 107, 9964-9972

[25] Talley CE, Jackson JB, Oubre C,Grady NK, Hollars CW, Lane SM, Huser TR, Nordlander P, Halas NJ **2005** Surface-Enhanced Raman Scattering from Individual Au Nanoparticles and Nanoparticle Dimer Substrates *Nano Lett.* 5, 1569-1574

[26] Grabar KC,Freeman RG, Hommer MB, Natan MJ **1995** Preparation and Characterization Of Au Colloid Monolayers *Anal. Chem.* 67, 735-743

[27] Grabar KC, Smith PC, Musick MD, Davis JA, Walter DG, Jackson MA, Guthrie AP, Natan MJ **1996** Kinetic Control of Interparticle Spacing in Au Colloid-Based Surfaces: Rational Nanometer-Scale Architecture *J. Am. Chem. Soc.* 118, 1148-1153

[28] Wang H, Levin CS, Halas NJ **2005** Nanosphere Arrays with Controlled Sub-10-nm Gaps as Surface-Enhanced Raman Spectroscopy Substrates *J. Am. Chem. Soc.* 127, 14992-14993

[29] Lu Y, Liu GL, Lee LP **2005** High-Density Silver Nanoparticle Film with Temperature-Controllable Interparticle Spacing for a Tunable Surface Enhanced Raman Scattering Substrate *Nano Lett.* 5, 5-9

[30] Willets KA, Van Duyne RP 2007 Localized Surface Plasmon Resonance Spectroscopy and Sensing *Annu. Rev. Phys. Chem.* 58, 267-297

[31] Kelly KL, Coronado E, Zhao LL, Schatz GC **2003** The Optical Properties of Metal Nanoparticles: The Influence of Size, Shape, and Dielectric Environment *J. Phys. Chem. B* 107, 668-677

[32] Zhang P, Haslett TL, Douketis C, Moskovits M **1998** Mode Localization in Self-affine Fractal Interfaces Observed by Near-field Microscopy *Phys. Rev. B* 57, 15513-15518

[33] Stockman MI, Shalaev VM, Moskovits M,Botet R, George TF **1992** Enhanced Raman Scattering by Fractal Clusters: Scaleinvariant Theory *Phys. Rev. B* 46, 2821-2830

[34] Shalaev VM **1996** Electromagnetic Properties of Small-Particle Composites *Phys. Rep.* 272, 61-137

[35] Markel VA, Shalaev VM, Zhang P, Huynh W, Tay L, Haslett TL, Moskovits M, **1999** Near-field Optical Spectroscopy of Individual Surface-plasmon Modes in Colloid Clusters *Phys. Rev. B* 59, 10903-10909

[36] Brolo AG, Arctander E, Gordon R, Leathem B, Kavanah KL **2004** Nanohole-Enhanced Raman Scattering *Nano Lett.* 4, 2015-2018

[37] Genet C, Ebbesen TW **2007** Light in Tiny Holes *Nature* 445, 39-46

[38] Murray WA, Astilean S, Barnes WL **2004** Transition from Localized Surface Plasmon Resonance to Extended Surface Plasmon-polariton as Metallic Nanoparticles Merge to Form a Periodic Hole Array *Phys. Rev. B* 69, (165407-1)-(165407-7)

[39] Canpean V, Astilean S **2009** Extending Nanosphere Lithography for the Fabrication of Periodic Arrays of Subwavelength Metallic Nanoholes *Mater. Lett.* 63, 2520-2522

[40] Yu Q, Braswell S, Christin B, Xu J, Wallace PM, Gong H, Kaminsky D **2010** Surface-enhanced Raman Scattering on Gold Quasi-3D Nanostructure and 2D Nanohole Arrays *Nanotechnology* 21, 355301 (9pp)

[41] Menezes JM, Ferreira J, Santos MJL, Cescato L, Brolo AG **2010** Large-Area Fabrication of Periodic Arrays of Nanoholes in Metal Films and Their Application in Biosensing and Plasmonic-Enhanced Photovoltaics *Adv. Funct. Mater.* 20, 3918-3924

[42] Wood RW **1902** On a Remarkable Case of Uneven Distribution of Light in a Diffraction Grating Spectrum *Phil. Magm.* 4, 396-402

[43] Kretschmann E, Raether H **1968** Radioactive Decay of non-Radioactive Surface Plasmons Excited by Light *Z. Naturforsch.* 23A, 2135-2136

[44] Fowles GF **1975** Introduction to Modern Optics *Dover Publications, 7ed*

[45] Homola J, Yee SS, Gauglitz G **1999** Surface Plasmon Resonance Sensors: Review *Sensors and Actuators B* 54, 3-15

[46] Raether H **1988** Surface Plasmons on Smooth and Rough Surfaces and on Gratings *Springer-Verlag, Berlin* 111

[47] Otto A **1968** Excitation of Surface Plasma Waves in Silver by the Method of Frustrated Total Reflection *Z. Physik* 216, 398-410

[48] Cullen DC, Brown RG, Lowe CR **1987** Detection of Immune-complex Formation via Surface Plasmon Resonance on Gold-coated Diffraction Gratings *Biosensors* 3, 21 l-225

[49] Brolo AG, Gordon R, Leathem B, Kavanah KL **2004** Surface Plasmon Sensor Based on the Enhanced Light Transmission through Arrays of Nanoholes in Gold Films *Langmuir* 20, 4813-4815

[50] Ebbesen TW, Lezec HJ, Ghaemi HF, Thio T, Wolff PA **1998** Extraordinary Optical Transmission through Sub-wavelength Hole Arrays *Nature* 391, 667-669

[51] Raman CV, Krishnan KS **1928** A New Type of Secondary Radiation *Nature* 121, 501-502

[52] Le Ru EC, Etchegoin PG **2009** Principles of Surface-enhanced Raman Spectroscopy and Related Plasmonic Effects *Elsevier, Amsterdam*

[53] Ferraro JR, Nakamoto K **1994** Introductory Raman Spectroscopy *Academic Press, London*

[54] Born M, Wolf E **1999** Electromagnetic Theory of Propagation, Interference and Diffraction of Light *Cambridge University Press, 7ed*

[55] Moskovits M **2005** Surface-enhanced Raman Spectroscopy: a Brief Retrospective *J. Raman Spectrosc.*36, 485-496

[56] Chalmers JM, Griffiths P **2002** Handbook of Vibrational Spectroscopy *Wiley 1ed*

[57] Moskovits M **1985** Surface-enhanced Spectroscopy *Rev. Mod. Phys.* 57, 783-826

[58] Xu H, Xie L, Zhang H, Zhang J **2011** Effect of Graphene Fermi Level on the Raman Scattering Intensity of Molecules on Graphene *ACS Nano* 5, 5338-5344

[59] Fan M, Andrade GFS, Brolo AG **2011** A Review on the Fabrication of Substrates for Surface Enhanced Raman Spectroscopy and Their Applications in Analytical Chemistry *Analytica Chimica Acta* 693, 7-25

[60] Evanoff Jr. DD, Chumanov G **2005** Synthesis and Optical Properties of Silver Nanoparticles and Arrays *Chem. Phys. Chem 7*, 1221-1231

[61] Meyer SA, Le Ru EC, Etchegoin PG **2011** Combining Surface Plasmon Resonance (SPR) Spectroscopy with Surface-Enhanced Raman Scattering (SERS) *Anal. Chem.* 83, 2337-2344

[62] Meyer SA, Auguie B, Le Ru EC, Etchegoin PG **2012** Combined SPR and SERS microscopy in the Kretschmann configuration *J. Phys. Chem. A* 116, 1000-1007

[63] Yang Z, Li Q, Ren B, Tian Z 2011 Tunable SERS from Aluminium Nanohole Arrays in the Ultraviolet Region Chem. Commun. 47, 3909-3911

[64] Le Ru EC, Galloway C, Etchegoin PG **2006** On the Connection between Optical Absorption/Extinction and SERS Enhancements *Phys. Chem. Chem. Phys.* 8, 3083-3087

[65] Lee A, Andrade GFS, Ahmed A, Souza M, Coombs N, Turmarkin E, Liu L, Gordon R, Brolo AG, Kumacheva E **2011** Probing Dynamic Generation of Hot-Spots in Self-Assembled Chains of Gold Nanorods by Surface-Enhanced Raman Scattering *J. Am. Chem. Soc.*133, 7563-7570

[66] Anema J, Marthandam P, Gordon R, Brolo AG **2008** Enhanced Raman Scattering from Nanoholes in a Copper Film *J. Phys. Chem. C* 112, 17051-17055

[67] Brolo AG, Irish DE **1996** Adsorption and Orientation of Pyrazine on Silver Electrode: A SERS Study *Journal of Electroanalytical Chemistry and Interfacial Electrochemistry* 414, 183-196

[68] dos Santos DP, Andrade GFS, Temperini MLA, Brolo AG **2009** Electrochemical Control of the Time-dependent Intensity Fluctuations in Surface-enhanced Raman Scattering (SERS) *J. Phys. Chem. C*, 113, 17737-17744

[69] Jensen L, Schatz GC **2006** Resonance Raman Scattering of Rhodamine 6G as Calculated Using Time-Dependent Density Functional Theory *J. Phys. Chem. A*, 110, 5973-5977

Chapter 2: Experimental Procedures

2.1 Fabrication of Nano-aperture Arrays

Nano-aperture arrays of circular, bow-tie, and cross bow-tie shaped holes were fabricated using a FEI 235 focused ion beam (FIB) milling [1] and imaged by a field emission scanning electron microscope (SEM) present in the same system (dual beam instrument). Glass slides coated with a 5 nm thick chromium adhesion layer and a 100 nm thick gold layer were used. This kind of slide is commercially available from Evaporated Metal Films.

A set of patterns for the nano-aperture arrays with different periodicities (distances between the centers of the apertures) or tip-to-tip distances (between the triangles in the bow-ties and cross bow-ties) were designed. These patterns were adapted by the FIB to mill out the nano-aperture arrays at the center of the glass slide. Gallium ions inside the FIB equipment were accelerated to 30 keV, and the milling rate was set to 1.6 nm·µs^{-1} for gold with a beam current of 300 nA [1]. This high energy ion beam was focused on gold surface to generate the designed pattern. The top atoms were sputtered away by the Gallium ion until both the Au layer and Cr layer were drilled through [1].

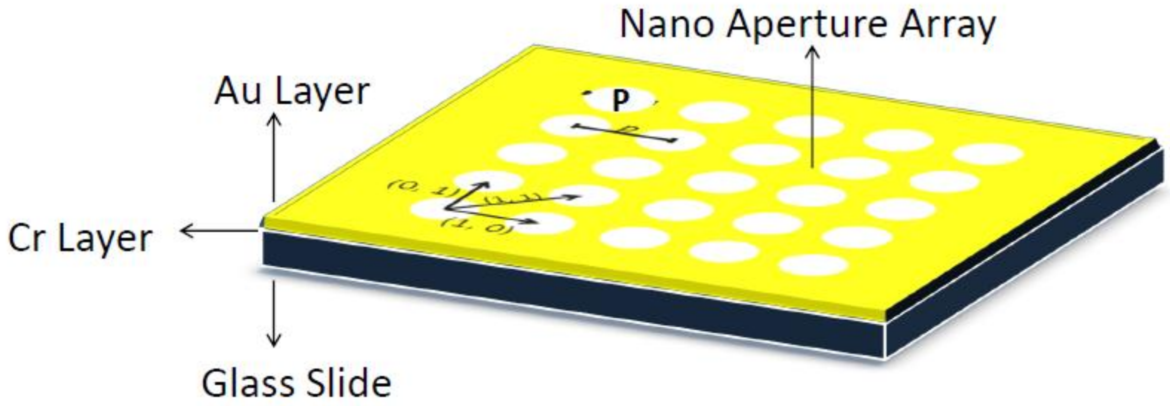

Figure 2.1 Schematic view of the glass slide bearing a nano-aperture array in its center. The thin adhesive layer of Cr was between the Au layer and the glass slide. Each white circle represents one nano-aperture unit. The distance between two neighbouring apertures is defined as the periodicity *p*. Three different diffractive modes, (0, 1), (1, 1) and (1, 0), are indicated in the figure.

Figure 2.1 shows the schematic view of the glass slide with a nano-aperture array. The location of the nano-aperture arrays (each with size about 2 μm × 2 μm) was designed to be at the center of the slide to make the spectroscopic measurements more convenient.

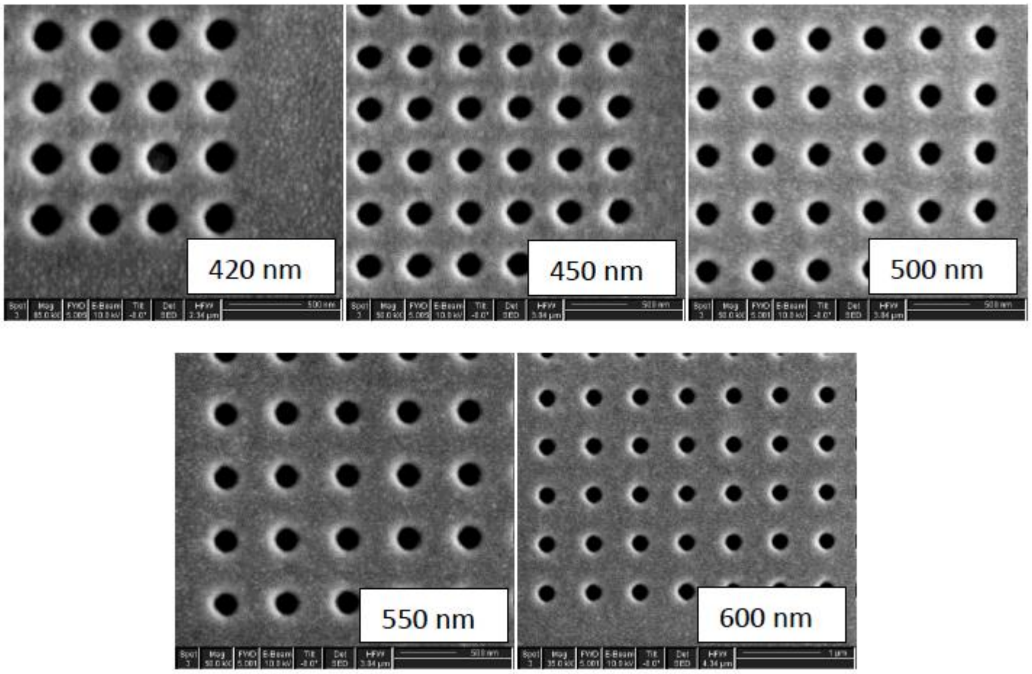

Figure 2.2 SEM images of the circular nano-aperture arrays with different periodicities ranging from 420 nm to 600 nm. The diameters for all the circular nano holes were ~200 nm.

Figure 2.2 shows the SEM images of circular nano-aperture arrays fabricated in this work. The grey granule texture is the gold layer, and all the nano holes appear in the SEM pictures as black circles. The sizes for all the nano holes were almost the same (200 nm in diameter) within 10%. The distance between the centers of two neighbouring nano-apertures (periodicity of the array) was designed to vary from 420 nm to 600 nm.

In bow-tie structure, two triangular apertures were placed with one tip facing the other. Each of these bow-tie structures constituted a unit of the nano-aperture array. For each structure, the lengths of all the triangular apertures were about 300 nm and the heights were about 150 nm within 10%. The distance between two triangular tips varies from -50 nm (overlapped) to 110 nm.

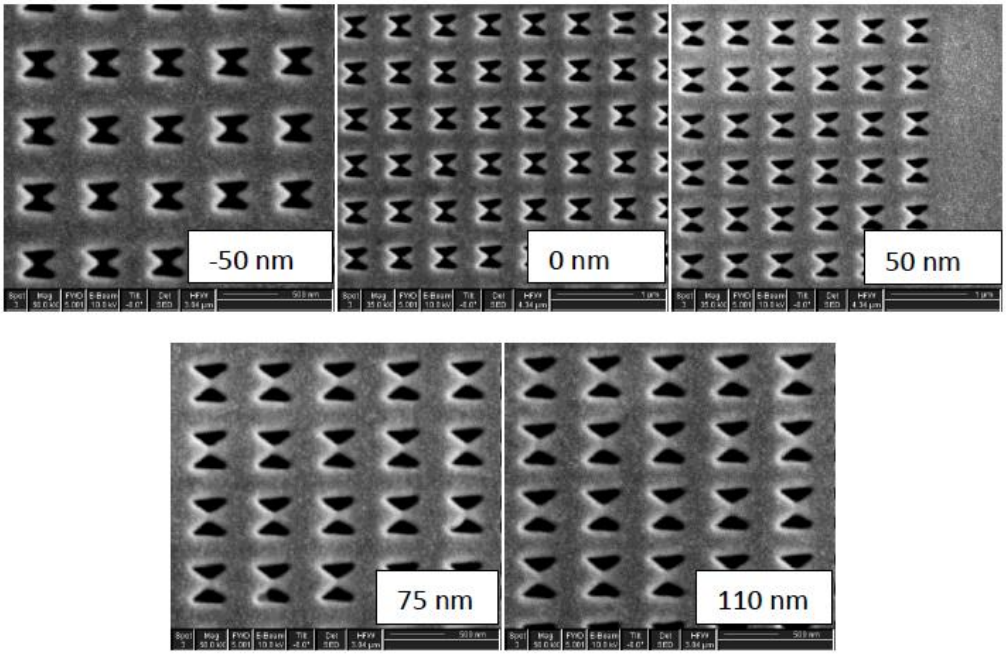

Figure 2.3 SEM images of the bow-tie nano-aperture arrays. All of them have the same 600 nm periodicity, but the tip-to-tip distance varied from -50 nm (overlapped) to 110 nm, as indicated in the images. The length of the bases of all triangular apertures was about 300 nm and the height of the triangle was about 150 nm within 10%.

Figure 2.3 shows the SEM images of the bow-tie nano-aperture arrays. The distance between two neighbouring units (center to center) was defined as the periodicity. All the five arrays shared the same periodicity, 600 nm. The tip-to-tip distance varied from -50 nm to 110 nm, as indicated in the figure.

The cross bow-tie nano-aperture was defined by four triangular apertures placed with one of their tips facing each other, and each structure was a unit in the nano-aperture array. Each triangle was designed to have the same shape and size, with the length of about 120 nm and height of about 120 nm within 15%. Similar to the bow-tie nano-aperture arrays, the tip-to-tip distances were varied. All the six arrays had the same 600 nm periodicity (center to center distance).

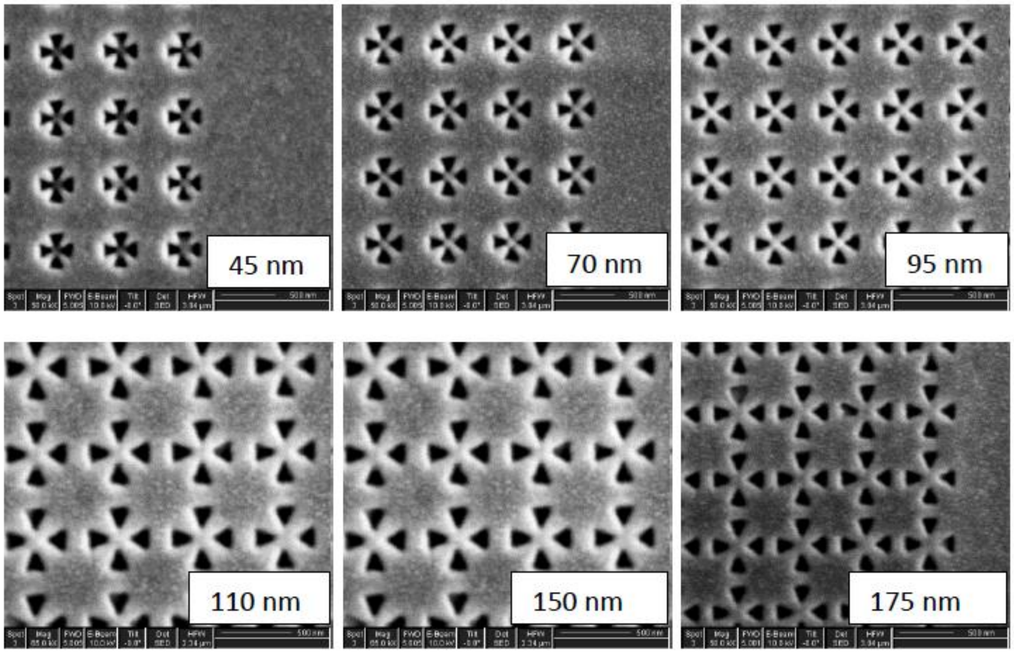

Figure 2.4 SEM images of the cross bow-tie nano-aperture arrays. The periodicity was the same for all arrays: 600 nm, but the tip-to-tip distances varied from 45 nm to 175 nm. The base lengths and heights of all the triangular apertures were about 120 nm.

Figure 2.4 shows the SEM of the cross bow-tie nano-aperture arrays fabricated in this work. The tip-to-tip distances were 45 nm, 70 nm, 95 nm, 110 nm, 150 nm and 175 nm, as indicated in Figure 2.4.

2.2 Preparation of Rhodamine 6G (R6G) Solution

Rhodamine 6G (CAS 989-38-8, Sigma-Aldrich) was used as the analyte probe molecule for all the Raman measurements. R6G was dissolved into a 0.1 M $KClO_4$ (CAS 7778-74-7, Aldrich) aqueous solution. The ionic solution was required for the electrochemical measurements.

2.3 Experimental Setup and Surface-enhanced Raman Scattering (SERS) Measurements

A spectro-electrochemical cell made of Teflon®, represented in Figure 2.5, was fabricated for all the SERS measurements [2].

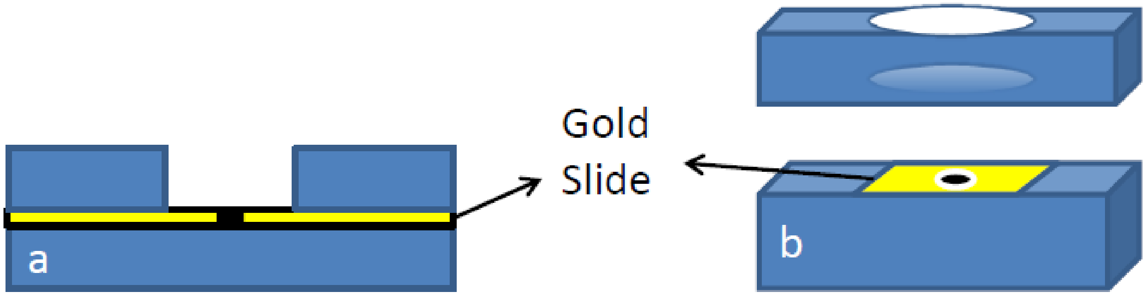

Figure 2.5 Schematic view of the spectro-electrochemical cell. The yellow square represents the SERS substrates. The black dot represents the nano-aperture array.

Figure 2.5 shows the schematic view of the spectro-electrochemical cell. Two pieces of Teflon and the gold slide were assembled together to form the cell. The gold slide was inserted in between the two well-sealed Teflon pieces. All the nano-aperture arrays, represented by the black circle in Figure 2.5, were designed to be located at the center of the gold slide, so they could also be at the center of the cell. The Teflon pieces were soaked in Piranha solution [3] for two hours prior to the experiments to remove any contamination. Each gold slide containing the nano aperture arrays was rinsed with methanol and then deionised water repeatedly before it was assembled into the cell. The cell was then placed in the translational stage of the Raman microscope for the measurements.

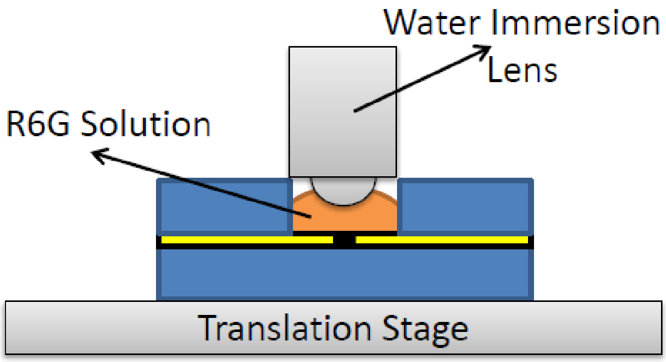

Figure 2.6 Schematic view of the experimental setup. The cell was placed on a piezo-controlled translation stage. The orange part with a meniscus represents the R6G solution in contact to the microscope objective. The water immersion objective lens was in contact to the solution and was used to focus the laser onto the nano-aperture arrays.

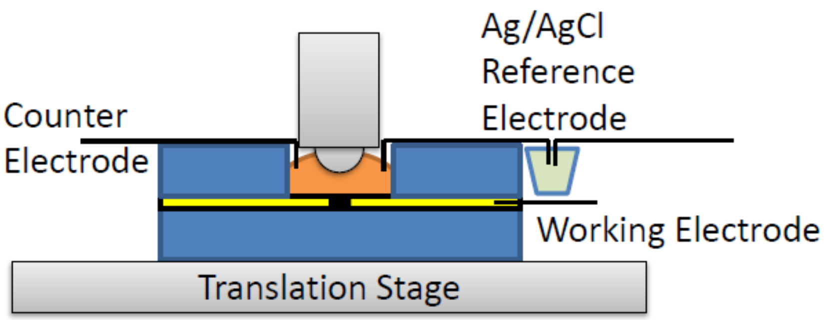

Figure 2.7 Schematic view of the analytical setup with electrochemical application. Three electrodes, a counter electrode, a working electrode and a Ag/AgCl reference electrode were assembled into the system.

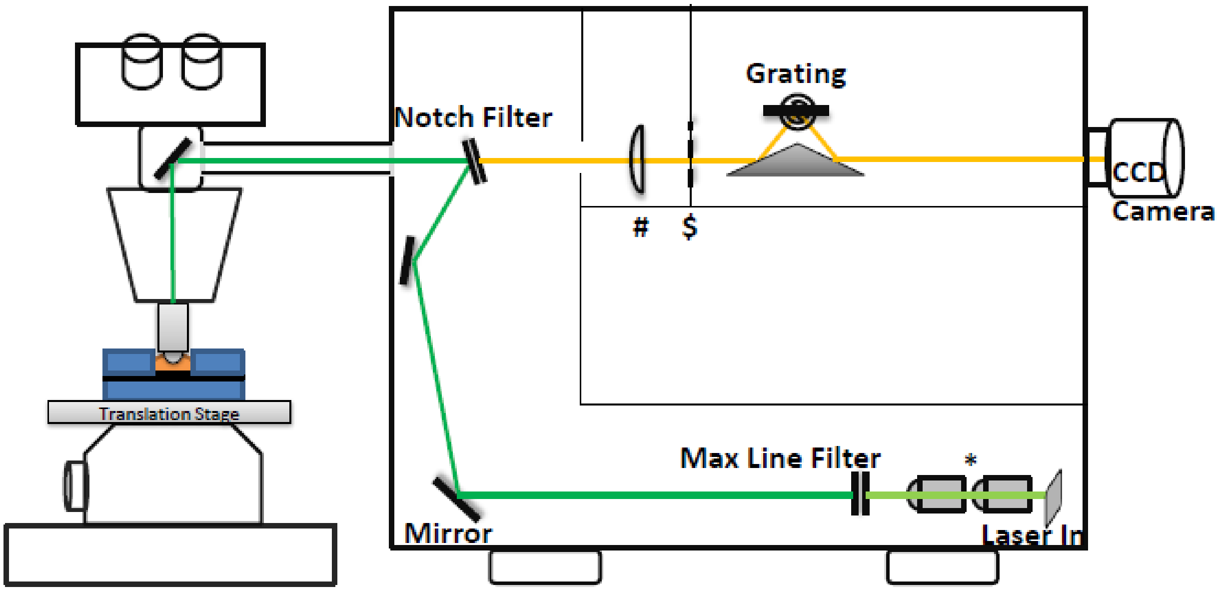

Figure 2.8 Schematic view of the RENISHAW inVia Raman microscope system. * represents the spatial filter. # represents lens that will focus the scattered light into the CCD chip. $ represents the entrance slit. Green laser was used as the incident excitation in this schematic and the orange light represents the scattered signal that was collected.

Figure 2.6 shows the setup for the SERS measurement. Figure 2.7 shows the setup for the experiments under electrochemical conditions. The same cell was used in this case, but electrodes were introduced to allow potential control at the gold surface. The counter electrode was a piece of platinum wire. The working electrode was the gold surface containing the nano-aperture arrays. A platinum wire was used to contact the gold surface to the potentiostat. The reference electrode was a piece of silver wire coated with AgCl in contact to a saturated KCl solution. This electrode was external to the cell to avoid contamination, but it got contact with analyte solution through a platinum wire. These electrodes were connected to a HAB-151 Hokuto-Denko potentiostat/galvanostat.

Raman spectroscopy measurements were carried out using a RENISHAW in Via Raman microscope system. Figure 2.8 shows a schematic for the setup of the Renishaw system for the SERS measurement. The laser introduced into the system is first focused by the beam shaping focus lens *. The laser is then directed to the microscope by a series of mirrors and a notch filter to illuminate the sample located at the microscope stage. The light scattered from the cell is collected by the microscope system through the same objective used for excitation. The notch filter removes the Rayleigh scattered light and the reflected incident light from the inelastic scattered signal. The Raman scattered light is focused through the focusing optics # and slit $ and dispersed in a grating where the scattered light is separated and the spectrum is recorded by the CCD camera. In this work, the Raman signal collected was the Stokes scattered light. The intensity of the signal was plotted against the Raman shift, which is the difference between the energy of the incident excitation and the Stokes scattered light in wavenumber (cm^{-1}) [4].

A He-Ne laser with excitation wavelength of 632.8 nm was equipped with the Raman microscope system. A 63X (NA=0.75) water immersion objective lens was used to both focus the laser spot (with size of ~3 μm^2) on the nano-aperture array and to collect the scattered photons. Each spectrum was taken with 3 s of illumination and one time accumulation.

For SERS measurement under electrochemical conditions, each spectrum was taken under the desired electrochemical potential applied by the potentiostat. Time series of SERS spectrum was also taken under the same procedure, but with 1 second interval between each collection. Three thousands spectra were taken for each time series data. The Raman intensity data of the time series spectra was preceded in the PCA procedure performed by the R x64 2.12.2 software [5]. All the SERS spectra were treated using Origin 8.5 to remove the baseline (except the time series data), and the height of each Raman peak was selected to represent its intensity.

2.4 White Light Transmission Spectroscopy

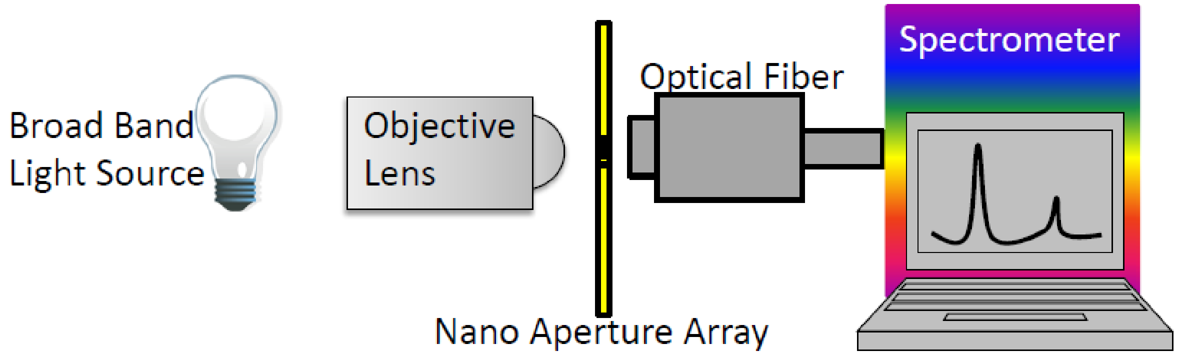

Figure 2.9 Schematic view of the experimental setup used for the white light transmission spectroscopy.

Figure 2.9 shows the schematic of the setup for white light transmission spectroscopy. A 100 W halogen lamp was used as the broad band light source. The experiments were realized using an Olympus BHSM metallurgical microscope system. The light was focused on the nano-aperture arrays using a 10X (NA=0.25) objective. The light transmitted through the aperture arrays was collected by an optical fiber and directed to an Ocean Optics USB-2000 handheld spectrometer.

The raw white light transmission spectra had contributions from the dark noise and from the gold layer transparency (caused by the interband sp-d transition which results in a sharp peak at 490 nm [6]). For each experiment, a spectrum collected in the dark (halogen light source off) was obtained and used to subtract the dark noise and a spectrum of a gold film without the nano-aperture arrays was used to subtract the gold layer transparency contribution. After those corrections, each transmission spectrum was transformed into transmittance using the following procedure: a white light transmission background spectrum was obtained using a gold slide with a single large aperture (same area as the whole array) and all the spectra from the nano-aperture arrays were normalized using the background spectrum and their fill factor.

2.5 Others

FDTD simulation (Lumerical FDTD Solutions software hosted by the Westgrid high performance computer cluster) based on solving the Maxwell's equation is adapted to simulate both the optical transmission and near field enhancement results [7]. This simulation was provided by Prof. Walter Salcedo from University of Sao Paulo.

Reference:

[1] Brolo AG, Gordon R, Leathem B, Kavanah KL **2004** Surface Plasmon Sensor Based on the Enhanced Light Transmission through Arrays of Nanoholes in Gold Films *Langmuir* 20, 4813-4815

[2] Fleischman M, Hendra PJ, McQuillan AJ **1974** Raman-Spectra of Pyridine Adsorbed at a Silver Electrode *Chem. Phys. Lett.* 26, 163-166

[3] Qiao H "Piranha Etch" Guide AMPEL Nanofabrication Facility, University of British Columbia #http://www.enotes.com/topic/Piranha_solution#

[4] Ferraro JR, Nakamoto K **1994** Introductory Raman Spectroscopy *Academic Press, London*

[5] dos Santos DP, Andrade GFS, Temperini MLA, Brolo AG **2009** Electrochemical Control of the Time-dependent Intensity Fluctuations in Surface-enhanced Raman Scattering (SERS) *J. Phys. Chem. C*, 113, 17737-17744

[6] Canpean V, Astilean S **2009** Extending Nanosphere Lithography for the Fabrication of Periodic Arrays of Subwavelength Metallic Nanoholes *Mater. Lett.* 63, 2520-2522

[7] Taflove A, Hagness SC **2000** Computational Electrodynamics: The Finite-Difference Time Domain Method *Artech House: Boston 2Ed*

Chapter 3: White Light Transmission Characterization of Nano-aperture Arrays

In this chapter, the surface plasmon resonance properties of different nano-aperture arrays were characterized by white light transmission spectroscopy. The experiments were realized using a microscope equipped with a broad band light source, coupled through a fiber optics to a handheld spectrometer. The spectra were then manipulated to remove the background from the environment and from light transmitted directly through the gold layer. A detailed description of the experimental setup and data manipulation is given in Chapter 2.

The white light transmission characterization was used to determine the resonance properties of the nano-aperture arrays. When the white light gets transmitted through the nano-aperture arrays, only certain wavelengths will be enhanced. The enhanced transmission at certain wavelengths is related to their periodicity and to the shape of the nanoholes [2, 8, 10].

3.1 Transmission Results for Arrays of Circular Nano-apertures

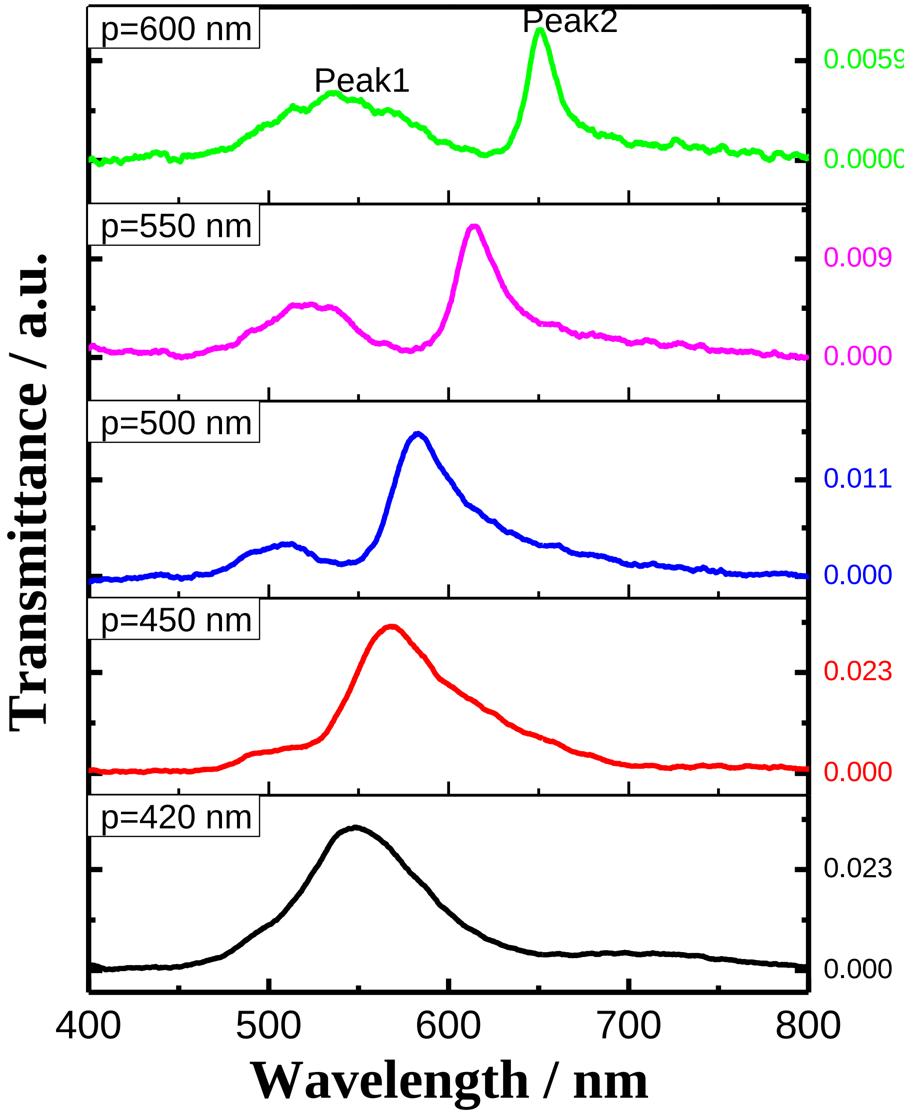

Figure 3.1 White light transmission spectra through circular nano-aperture arrays with different periodicities. As descripted in Section 2.1, Chapter 2, all the nano-apertures were drilled in 100 nm-thick gold films. The diameters of the nanoholes were about 200 nm. The periodicities of arrays were 420 nm, 450 nm, 500 nm, 550 nm, and 600 nm respectively. The lower wavelength peak is called Peak1 in the text and the peak with a higher wavelength is called Peak2.

Table 3.1 Resonance wavelengths of white light transmission peaks for circular nano-aperture arrays.

Periodicity/ nm	Peak1/ nm	Peak2/ nm
420	*	547
450	492	569
500	510	583
550	524	614
600	537	651

*Peak1 is not identifiable for the circular nano-aperture array with 420 nm periodicity.

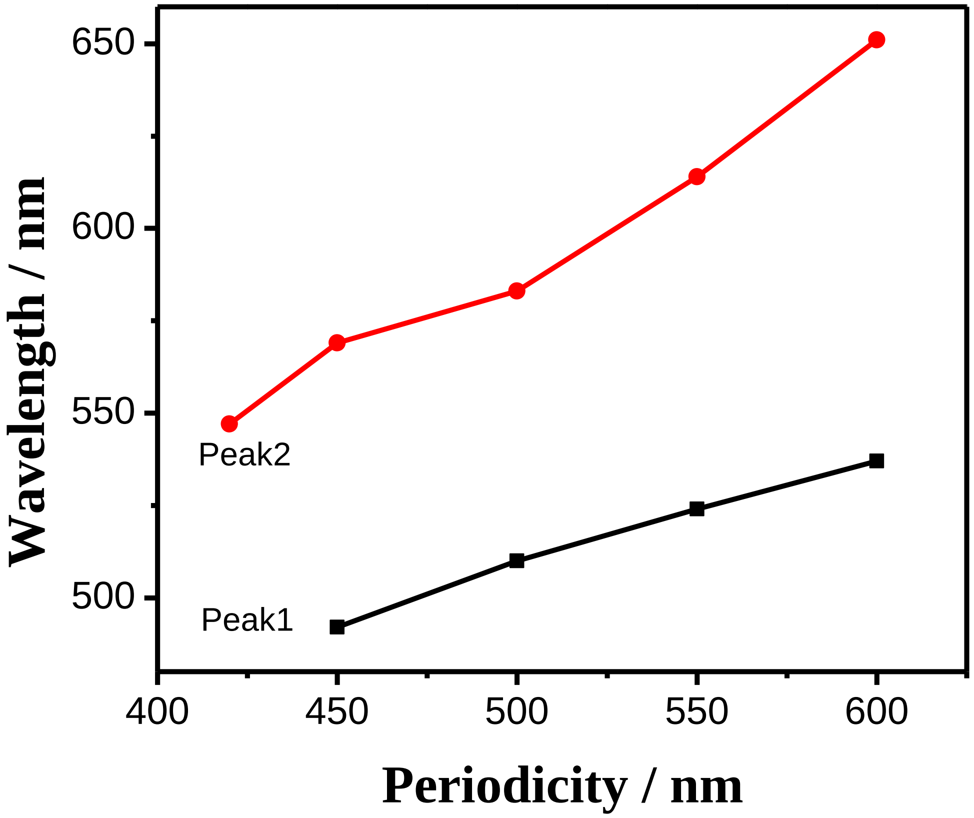

Figure 3.2 White light transmission peaks through circular nano-aperture arrays with periodicities ranging from 420 nm to 600 nm. Peak1 is the shorter wavelength, and peak2 is the longer wavelength.

Figure 3.1 shows the white light transmission spectra for several arrays of circular nano-apertures in gold film with the same diameter but different periodicities. As it can be seen from the spectral data in Figure 3.1, two typical transmission peaks are generally observed in the visible range. All the peaks of transmission are listed in Table 3.1 and plotted against the periodicity of the arrays in Figure 3.2. Nano-aperture array with a larger periodicity, *p*, will produce SP wave at a higher wavelength. The red-shift of the transmission peaks against the periodicity changes is in accordance to Equation 3.1.

Periodic nano-aperture arrays in metal films will allow the conditions for surface plasmons (SP) excitation to be achieved [1]. A consequence of the surface plasmon resonance (SPR) condition is the enhanced transmission of light through the nano-apertures at certain wavelengths, a phenomenon known as "extraordinary optical transmission" (EOT) [2], as mentioned in Section 1.3.2, Chapter 1.The SPR condition for light transmitted through a square array of circular nano-apertures is given by Equation 3.1 [1, 2] below:

$$\lambda^{SP}(i,j) = p(i^2 + j^2)^{-1/2}\left(\frac{\epsilon_{eff}\epsilon_m}{\epsilon_{eff}+\epsilon_m}\right)^{1/2} \qquad (3.1)$$

In this equation, *p* is the periodicity of the circular nano-aperture array, *i* and *j* are integers that represent the order of the resonance, ϵ_{eff} is the effective permittivity at the metal-dielectric interface, and ϵ_m is the real part of the permittivity of the metal.

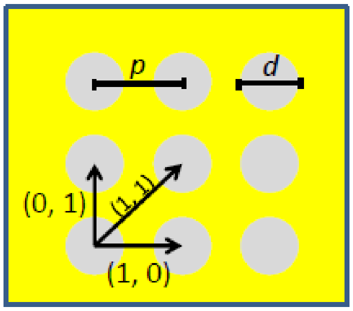

Figure 3.3 Cartoon defining the diameter, *d*, periodicity, *p* and SP propagation modes for a square array of circular nano-apertures.

There are two possible reasons for the origin of these two peaks. They can be either concerned with the different Bragg orders of the SPR propagation, or with the SPR from the Au-glass and Au-air interfaces, respectively. These two possibilities will be explored next.

Figure 3.3 illustrates the different SP propagation modes for a square array of circular nano-apertures. When the SP is excited, it propagates between the apertures. In the case of a square array, the propagation direction could follow the edge of the square unit lattice. When the Bragg condition is satisfied for neighbouring holes, the SP mode is assigned as (1, 0) or (0, 1). On the other hand, if the propagation is through the diagonal of the square unit lattice and the resonance condition is satisfied for neighbouring holes, the SP mode is assigned as (1, 1). Other diffraction orders for the integers i and j in Equation 3.1 are obtained when the Bragg condition involves nanoholes that are more than one lattice unit of distance from each other. However, these modes would result in decreased transmission intensity due to the localization property of the SPR [3, 4].

Table 3.2 Permittivity of gold for different wavelengths at 20˚C [5, 6, 15].

Wavelength/ nm	**472**	**479**	**486**	**499**	**502**	**507**	**510**	**515**	**524**	
n	1.292	1.205	1.086	0.87	0.825	0.751	0.706	0.632	0.54	Continued
k	1.809	1.801	1.817	1.881	1.922	1.990	2.030	2.098	2.258	
$\epsilon_m = n^2 - k^2$	-1.606	-1.792	-2.122	-2.784	-3.015	-3.396	-3.626	-4.004	-4.810	
$(\frac{\epsilon_{eff}\epsilon_m}{\epsilon_{eff}+\epsilon_m})^{1/2} Air$	1.628	1.504	1.375	1.249	1.223	1.190	1.175	1.154	1.124	
$(\frac{\epsilon_{eff}\epsilon_m}{\epsilon_{eff}+\epsilon_m})^{1/2} Gl.$	5.032	3.100	2.288	1.817	1.739	1.649	1.609	1.557	1.484	
	542	**552**	**559**	**577**	**599**	**602**	**636**	**661**	**724**	**765**
n	0.390	0.351	0.324	0.285	0.250	0.245	0.192	0.165	0.163	0.172
k	2.581	2.719	2.816	2.920	2.987	2.996	3.099	3.301	4.278	4.749
$\epsilon_m = n^2 - k^2$	-6.509	-7.274	-7.830	-8.450	-8.863	-8.920	-9.573	-10.88	-18.28	-22.53
$(\frac{\epsilon_{eff}\epsilon_m}{\epsilon_{eff}+\epsilon_m})^{1/2} Air$	1.087	1.077	1.071	1.065	1.062	1.061	1.057	1.049	1.029	1.023
$(\frac{\epsilon_{eff}\epsilon_m}{\epsilon_{eff}+\epsilon_m})^{1/2} Gl.$	1.402	1.380	1.368	1.356	1.349	1.348	1.339	1.324	1.283	1.272

Gl. is short for glass.

Table 3.2 shows the permittivity for gold at different wavelengths and at the temperature of 20˚C. In this table, *n* is the index of refraction of gold, and *k* is the gold extinction coefficient. The real part of the gold's permittivity ϵ_m can be calculated as n^2-

k^2, and it becomes more negative as the wavelength increases. The results of calculated $(\frac{\epsilon_{\mathrm{eff}}\epsilon_{\mathrm{m}}}{\epsilon_{\mathrm{eff}}+\epsilon_{\mathrm{m}}})^{1/2}$ term for both Au-Air ($\epsilon_{\mathrm{eff}} = 1$) and Au-Glass ($\epsilon_{\mathrm{eff}} = 1.51$) interfaces are also shown in Table 3.2.

If both Peak1 and Peak2 are considered to be from the gold-air interface, then the long wavelength peak (Peak2) should be assigned to the (1, 0) mode and the blue shifted peak (Peak1) should be due to the (1, 1) mode. Then the wavelengths of the resonance peaks could be calculated using Equation 3.1. There are other considerations. First, both peaks could be from gold-glass interface with the longer wavelength Peak2 assigned to the (1, 0) mode and the shorter wavelength Peak1 to the (1, 1) mode. Second, it could be possible that the two peaks are the same resonance mode (both (1, 0) or (1, 1) mode), but from different interfaces. Therefore, all these possible resonance peak modes (Au-Air (1, 0), Au-Air (1, 1), Au-Glass (1, 0), Au-Glass (1, 1)) have been calculated using in Equation 3.1 and the results are summarized in Table 3.3.

Table 3.3 Wavelengths of resonance peak calculated with Equation 3.1 for the gold-air interface and gold-glass interface with (1, 0) or (1, 1) mode.

Periodicity/ nm	**Peak1 / nm**	**Peak2 / nm**	**Au-Air (1, 1)**	**Au-Air (1, 0)**	**Au-Gl. (1, 1)**	**Au-Gl. (1, 0)**
420	*	547	*472	502	*502	559
450	492	569	479	515	510	602
500	510	583	486	542	524	661
550	524	614	499	599	552	724
600	537	651	507	636	577	765

*For the circular nano-aperture array with 420 nm periodicity, the two peaks overlapped. Gl. is short for glass.

Table 3.3 shows the calculated results from Equation 3.1 for all the possible resonance peaks. Compared to the experimental results, the Au-Air (1, 1) mode can be assigned to Peak1 and the Au-Air (1, 0) mode is related to Peak2. The Au-Gl. (1, 0) mode occurs at wavelengths that are far away from the experimental results, thus it is unlikely related to the experimental Peak1 or Peak2. The other possibility is that both Peak1 and Peak2 are from the (1, 1) SP mode, with Peak1 from the Au-Air interface and Peak2 from the Au-Glass interface.

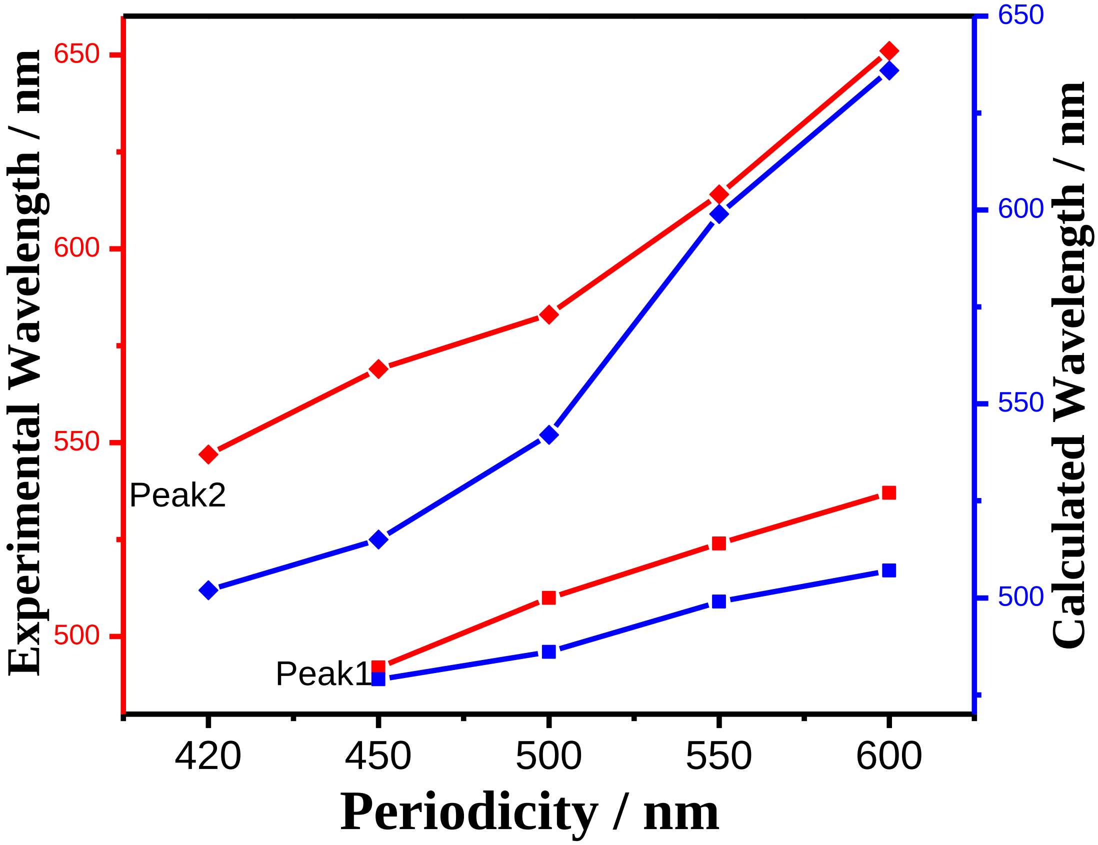

Figure 3.4 Comparison of resonance peaks between experimental result and calculated result (Au-Air interface (1, 0) and (1, 1) modes) from Table 3.3.

Figure 3.4 shows a comparison of the SP resonance trend between the experimental and the calculated results considering that the gold-air (1, 1) mode is the Peak1 and the gold-air (1, 0) mode is the Peak2. Although the calculated wavelengths are normally smaller than the experimental results, both present the same trend as the periodicity of the circular nano-aperture array changes. For Peak1, a close relationship is found between the experimental results and the calculated for the gold-air (1, 1) mode from Equation 3.1. While for the high wavelength peak (Peak2), there is a disagreement for the smaller periodicities, but a close agreement is observed for longer periodicity.

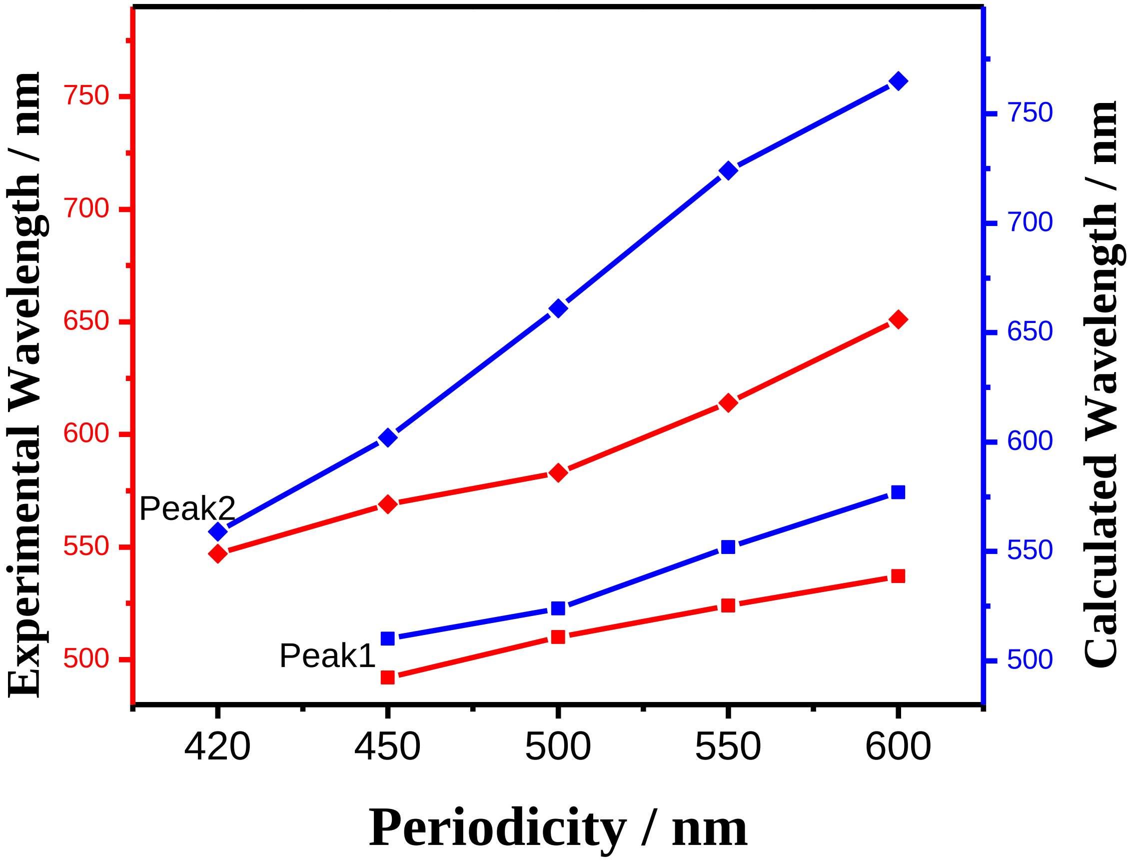

Figure 3.5 Comparison of resonance peaks between experimental and calculated results (Au-Glass interface (1, 0) and (1, 1) modes) from Table3.3.

Figure 3.5 shows another possible origin of the SP peaks. A comparison of the SP resonance trend between the experimental and the calculated results considering that the gold-glass (1, 1) mode is the Peak1 and the gold-glass (1, 0) mode is the Peak2 is provided. For Peak1, a close relationship is found between the experimental results and the calculated for the gold-glass (1, 1) mode from Equation 3.1. While for the high wavelength peak (Peak2), there is a disagreement for the longer periodicities, but a close agreement is observed for smaller periodicity.

Figure 3.4 and Figure 3.5 show that the use of Equation 3.1 does not allow a definitive assignment for both Peak1 and Peak2. This is because Equation 3.1 just considers the Bragg resonance of the arrays and is generally used as a first approximation for peak assignment.

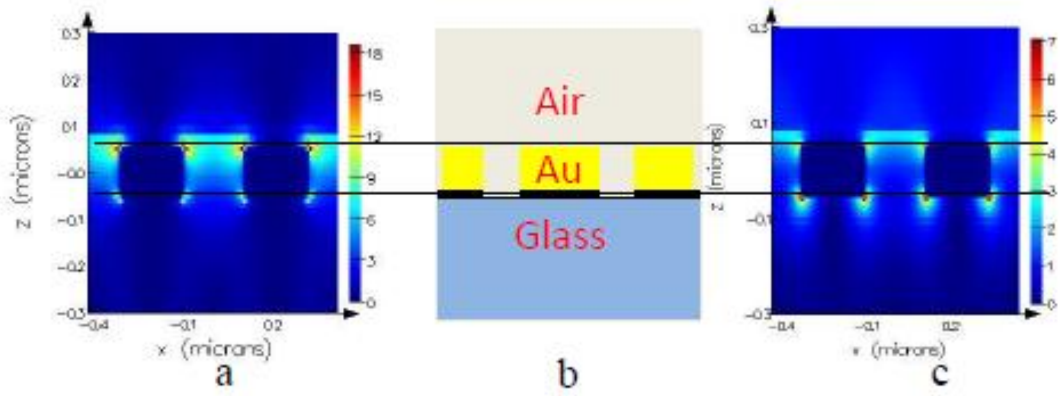

Figure 3.6 FDTD simulation of (a) (1, 1) SPR mode at the gold-air interface; and (c) (1, 0) SPR mode at both the gold-air and gold-glass interface. (b) Schematic of the air-gold-glass configuration of the samples. The bold black line between the gold and the glass represents the chromium adhesion layer.

Comprehensive numerical simulations were required in order to assign the two peaks observed in the transmission spectra. The simulations were carried out for all the periodicities indicated in Table 3.1. Every calculated transmitted spectrum yielded two peaks in the visible range, in accordance with the experimental results shown in Figure 3.1. Figure 3.6a shows the FDTD simulation of the electric field profile for Peak1 at 573 nm and Figure 3.6c shows the field profile for Peak2 at 695 nm. For all the periodicities, the simulation for Peak1 shows a field distribution that is dominated by the gold-air interface. Therefore, it is possible to be concluded that this mode has a strong contribution from the gold-air (1, 1) resonance and not from the gold-glass interface, as shown in Figure 3.6a. The FDTD simulation of the mode for peak 2, however, consistently showed for different periodicities that the mode has contributions from both the gold-air and the gold-glass interfaces, as shown in Figure 3.6c. This indicates that Peak2 has contributions from both interfaces and can be the hybrid of both. There are reports in the literature that indicate the chromium adhesion layer between the gold film and glass quenches the SPR at the gold-glass interface [7]. This might explain the absence of the gold-glass contribution in Peak1, although the simulation clearly indicate and gold-glass contribution to Peak2.

As a first approximation, the maximum transmission peak position provides a way to select the most appropriate incident laser for SERS in circular nano-aperture arrays.

However, in practice, the laser excitation is fixed by the Raman instrumentation, since SERS experiments are generally performed using cw, non-tunable, laser sources. The overall transmittance intensity at the laser wavelengths of our particular instrument would then be the proper parameter to estimate the SERS efficiency. Considering, for instance, the 632.8 nm wavelength of a typical He-Ne laser, a commonly used excitation source in Raman spectroscopy, it is possible to predict which array would be a best SERS substrate for that particular excitation. Notice that, in order to compare different arrays of nano holes, the transmittance intensities at the laser wavelength have to be corrected to account for the variation in the open area of the structure with the periodicity. This is done by correcting the transmission intensities by the fill factor, presented in Table 3.4.

Table 3.4 Geometric characteristics of the circular nano-aperture array investigated.

Periodicity/ nm	Diameter/ nm	Distance X×Y/ nm^2	Fill Factor/ %
420	209	400*418	20.5
450	197	434*459	15.3
500	183	491*509	10.5
550	194	557*573	9.3
600	197	590*613	8.4

Table 3.4 shows the geometric characteristics of the circular nano-aperture arrays. This includes the measured diameter of the nano-hole and the measured distance between the neighbouring nano-holes' centers from SEM images. The array can be viewed as the assembly of one individual square with a hole punched in the middle. And the area ratio between the hole and the square is called Fill Factor.

Figure 3.7 shows the transmittance intensities for all the circular nano-aperture arrays at the wavelengths of 633 nm and 785 nm (the other laser source in our Raman microscope setup). All the intensities have been normalized according to the fill factor listed in Table 3.4 [8]. Although the circular nano-aperture array with 550 nm periodicity has the SPR peak closest to 633 nm, its transmittance at 633 nm is still lower than that from the 450 nm periodicity array. This is due to the overall low transmittance intensity of the 550 nm periodicity array. For array with 420 nm periodicity, although the overall transmittance is very high, its SPR peak at 455 nm is too far away from 633 nm. The situation at 785 nm wavelength is also showed in Figure 3.7. In this case, the SPR peaks from all the arrays are far from 785 nm, although the transmittance at 785 nm for the arrays with 420 nm and 450 nm periodicities are higher than for the other arrays due to the overall high transmission efficiency observed for those samples. All these circular nano-aperture arrays were designed to be SERS substrates [9], and it is believed that the overlap between their SPR and the incident laser wavelength will be beneficial to their SERS enhancement properties [10]. However, the main parameters that actually need to be considered (in terms of electromagnetic enhancement), is the local electromagnetic field strength (hot spot efficiency). In another words, the maximum SERS enhancement factor does not necessarily correlate with the array with the best EOT effect [11, 12]. The white light transmission experiments provide a method to characterize the SPR effect and the effect of the array's periodicity. The relationship between the SPR, the local electromagnetic field, and the SERS property from each array will be discussed more thoroughly in the next chapter.

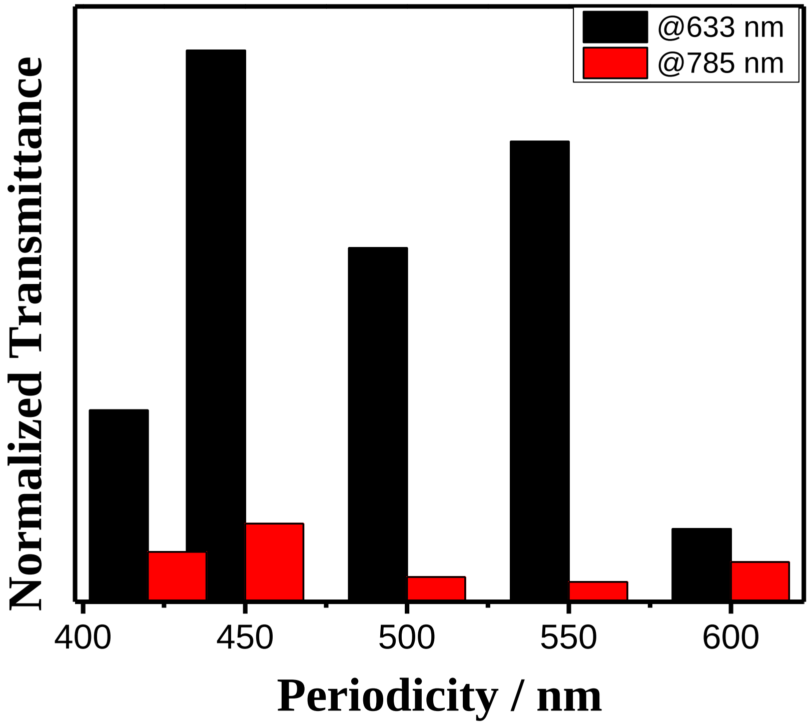

Figure 3.7 Normalized transmittance of at 633 nm and 785 nm for circular nano-aperture arrays with different periodicities.

3.2 Transmission Results for Arrays of Bow-tie Nano-apertures

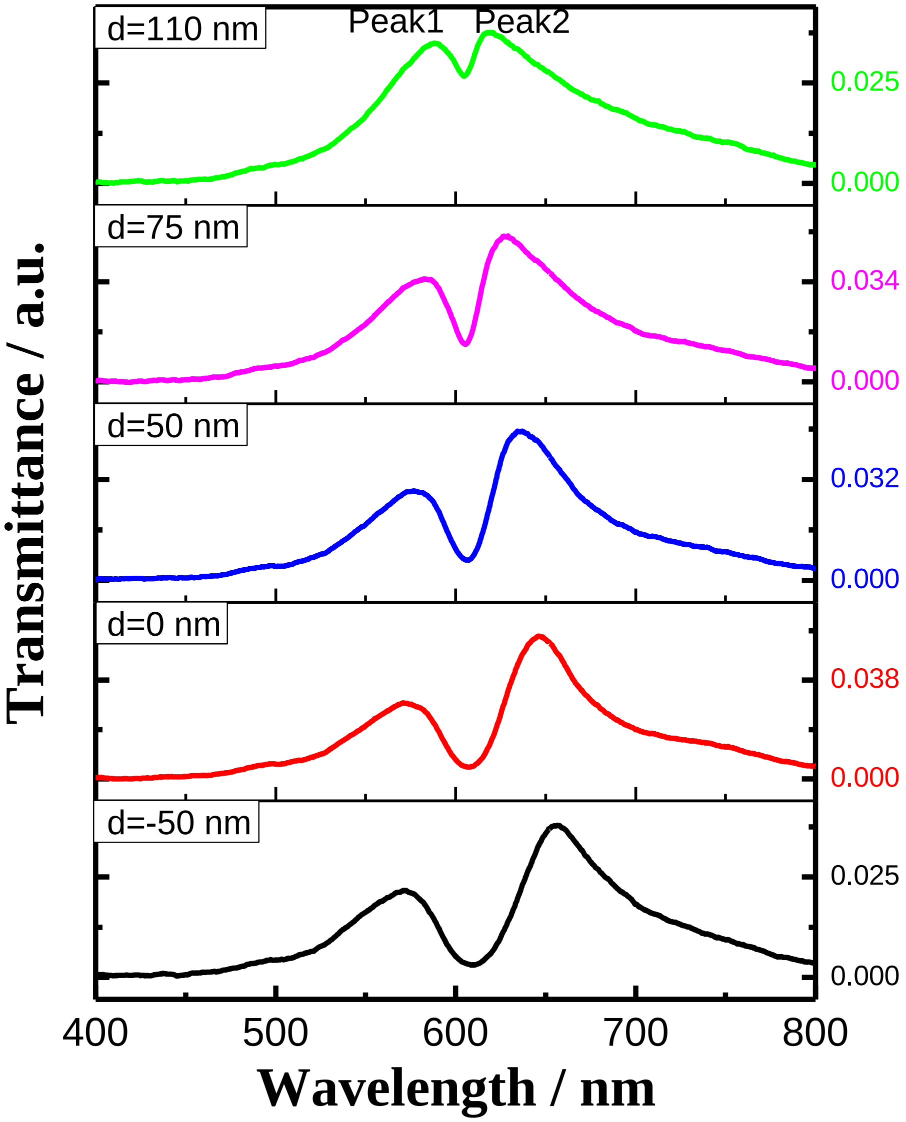

Figure 3.8 White light transmission spectra of bow-tie nano-aperture arrays with different tip-to-tip distances. As descripted in Section 2.1, Chapter 2, all these nano-apertures were drilled in gold films of 100 nm thickness. The base of the triangle was 300 nm and the corresponding height was 150 nm. The periodicities for all the arrays were the same, 600 nm. The tip-to-tip distances of the facing triangles were -50 nm (overlapped), 0 nm, 50 nm, 75 nm and 110 nm respectively. The peak with shorter wavelength was assigned as Peak1, and the other as Peak2.

Figure 3.8 shows the white light transmission spectra through different bow-tie nano-aperture arrays (the detailed geometric parameters of the arrays are given in Chapter 2). In this case, the periodicity of the arrays was maintained constant and only the tip-to-tip separation between the apertures was varied. Two transmission peaks (assigned as Peak1 and Peak2 in the figure) can be observed for each bow-tie nano-aperture array. Peak1 red-shifts with the increase of the tip-to-tip distance, while Peak2 blue-shifts. The peak positions for all the samples are listed in the following table.

Table 3.5 Resonance wavelengths of white light transmission peaks for bow-tie nano-aperture arrays with different tip-to-tip distances.

Tip-to-tip Distance/ nm	Peak1/ nm	Peak2/ nm
-50	571	656
0	572	646
50	577	636
75	582	627
110	587	618

In the case of circular nano-aperture arrays, the position of the SPR is explained using only the Bragg condition, given by the Equation 3.1. According to that equation, a square latticed structure with periodicity of 600 nm should present SPR (enhanced transmission) peaks at 537 nm and 651 nm. Although all the bow-tie nano-aperture arrays have the same 600 nm periodicity, the transmission peaks change with the relative positions between the triangles. This shows that the SPR for bow-tie nano-aperture arrays are not only due to the diffraction modes, but also depends on localized plasmonics modes in each bow-tie basis [13].

In order to interpret the transmission data, numerical studies using the finite-difference time-domain (FDTD) method was performed. The calculated white light transmission is shown in Figure 3.9. The experimental white light transmission spectra (Fig. 3.8) and the FDTD simulated transmission spectra (Fig.3.9) are in good qualitative agreement. They both present two transmission peaks that vary with tip-to-tip distance, following the same trend.

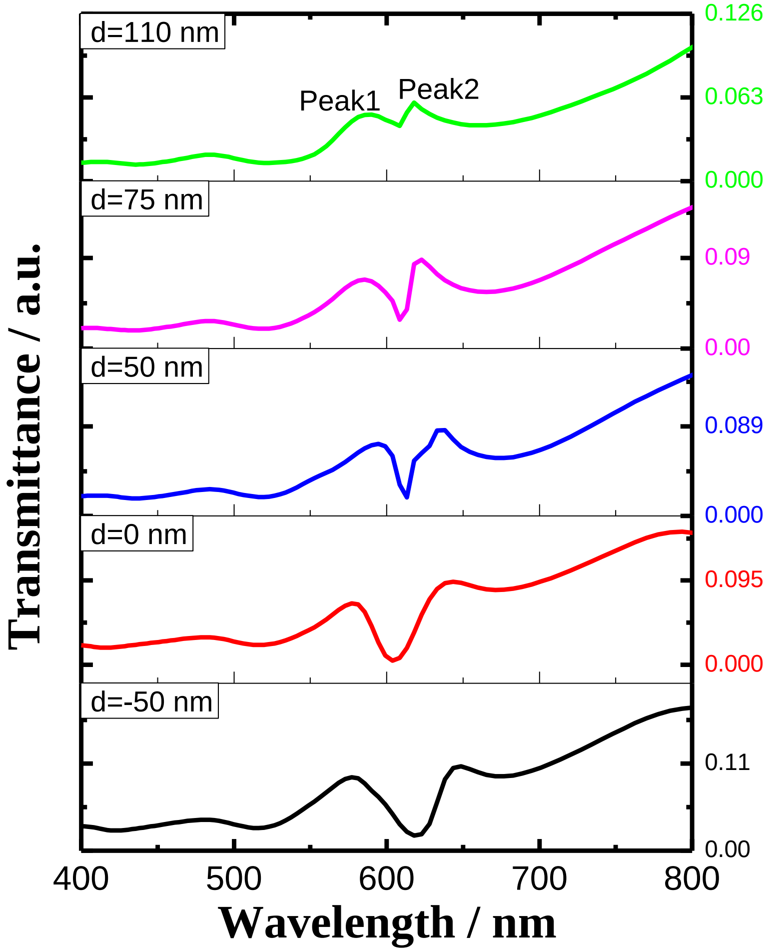

Figure 3.9 FDTD simulation results of white light transmission spectra through bow-tie nano-aperture arrays with different tip-to-tip distances.

Table 3.6 FDTD simulation results of white light transmission peak positions for bow-tie nano-aperture arrays.

Tip Distance/ nm	Peak1/ nm	Peak2/ nm
-50	577	649
0	577	643
50	595	638
75	586	623
110	590	618

Figure 3.9 shows the FDTD simulation results of the white light transmission of bow-tie nano-aperture arrays. Two typical transmission peaks can be observed from the

spectral data. The positions of all the resonance peaks are listed Table 3.6. All the peak positions from the experimental result and the FDTD simulation result are compared in Figure 3.10.

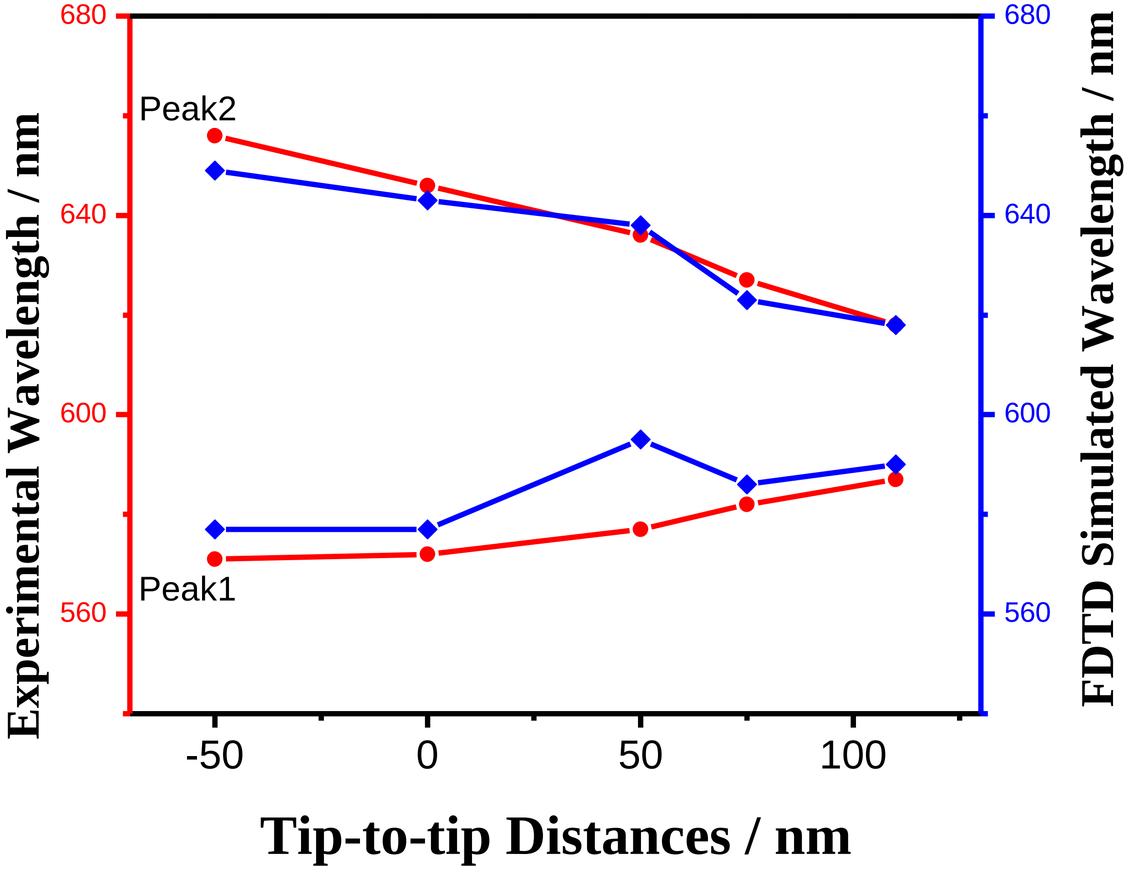

Figure 3.10 Comparison of resonance peaks between experimental and FDTD simulation results.

Figure 3.10 shows the comparison of resonance peaks between the experimental and the FDTD simulation results. A good agreement between experiment and calculation is observed both in terms of resonance peak positions and the trends relative to the tip-to-tip distance. Because the FDTD simulations are based on the interaction at the gold-air interface, this comparison shows that the resonance peaks are not originated from the gold-glass interface (see Figure 3.6).

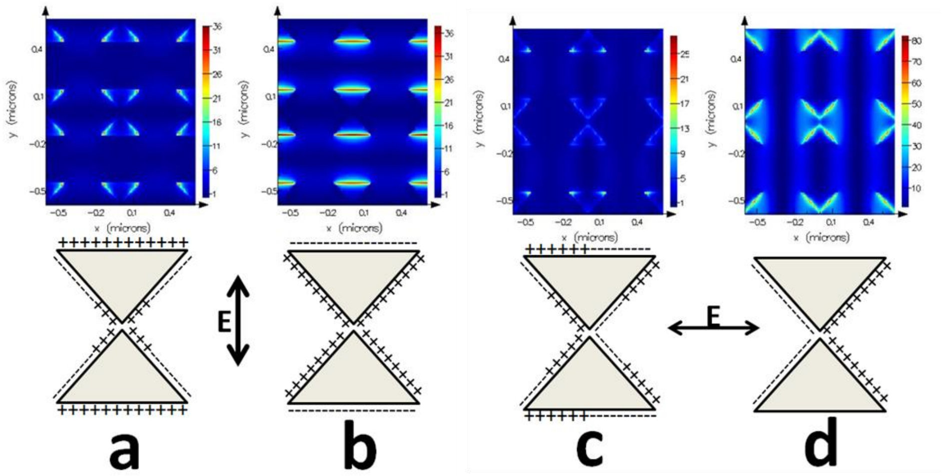

Figure 3.11 FDTD simulation of (a), (b), SPR at gold-air interface under parallel polarized light, and (c), (d), SPR at gold-air interface under perpendicular polarized light. The symbol – shows where the electrons are located and the symbol + shows where the holes are located. The locations of the electrons and holes change with the oscillating electromagnetic force.

Figure 3.11 shows the FDTD simulation of the possible SPR modes at the gold-air interface for the bow-tie nano-aperture arrays. In the case of circular nano-aperture arrays, the shape of the aperture is symmetric. However, the bow-tie aperture is anisotropic. This anisotropy results in different SPR modes excited under different polarization of the incident lights. The SPR modes (a) (Ez at 580 nm) and (b) (Ez at 640 nm) in Figure 3.11 are excited under a polarization parallel to the tip-to-tip separation, while the modes (c) (Ez at 594 nm) and (d) (Ez at 638 nm) are obtained under perpendicular incident light polarization (relative to the tip-to-tip separation, as indicated in the figure).

Table 3.7 Geometric characteristics of bow-tie nano-aperture arrays.

Tip-to-tip Distance/ nm	Aperture Area/ nm^2	Periodicity X*Y/ nm^2	Fill Factor/ %
-50	42940	582×602	12.3
0	40552	582×601	11.6
50	38178	597×616	10.4
75	37465	574×598	10.9
110	39087	597×622	10.5

Table 3.7 shows the geometric characteristics of the bow-tie nano-aperture arrays. This includes the measured area of the aperture and distance between neighbouring bow-tie, obtained from the SEM images. The array can be viewed as the assembly of one

individual square with a bow-tie shaped aperture punched in the middle. And the area ratio between the aperture and the square is called Fill Factor.

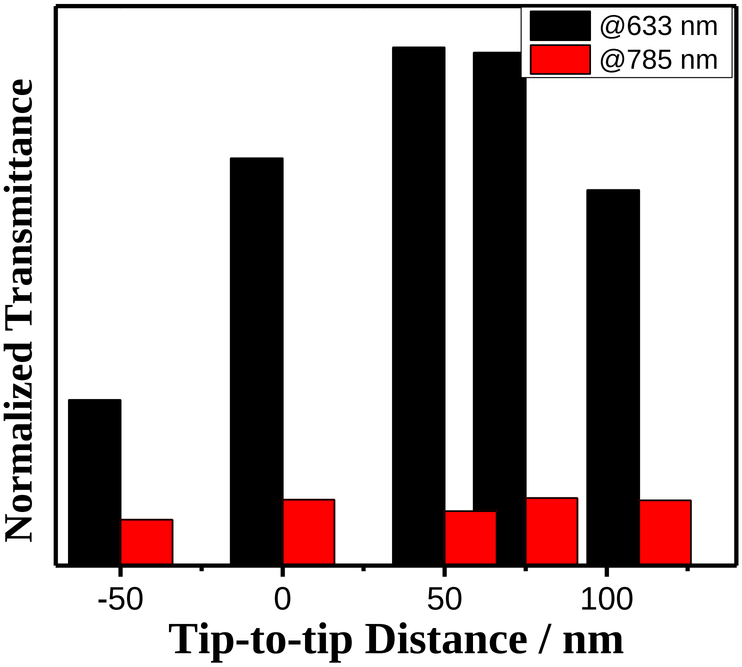

Figure 3.12 Normalized transmittance of white lights at 633 nm and 785 nm for bow-tie nano-aperture arrays with different tip-to-tip distances.

Figure 3.12 shows the white light transmittance intensities for all the bow-tie nano-aperture arrays at 633 nm and 785 nm wavelength. All the intensities have been normalized according to the fill factor listed in Table 3.7 [8]. All the arrays present white light transmittance at similar intensity level except the array with overlapped bow-tie aperture (d= -50 nm). The arrays with 50 nm and 75 nm tip-to-tip distances present relatively higher intensities at 633 nm wavelength. This can be attributed to the positions of their Peak2 resonances, which are both close to 633 nm. As all of the SPR peaks are far away from 785 nm, the transmittance intensities at this wavelength do not vary much between arrays.

3.3 Transmission Results for Arrays of Cross Bow-tie Nano-apertures

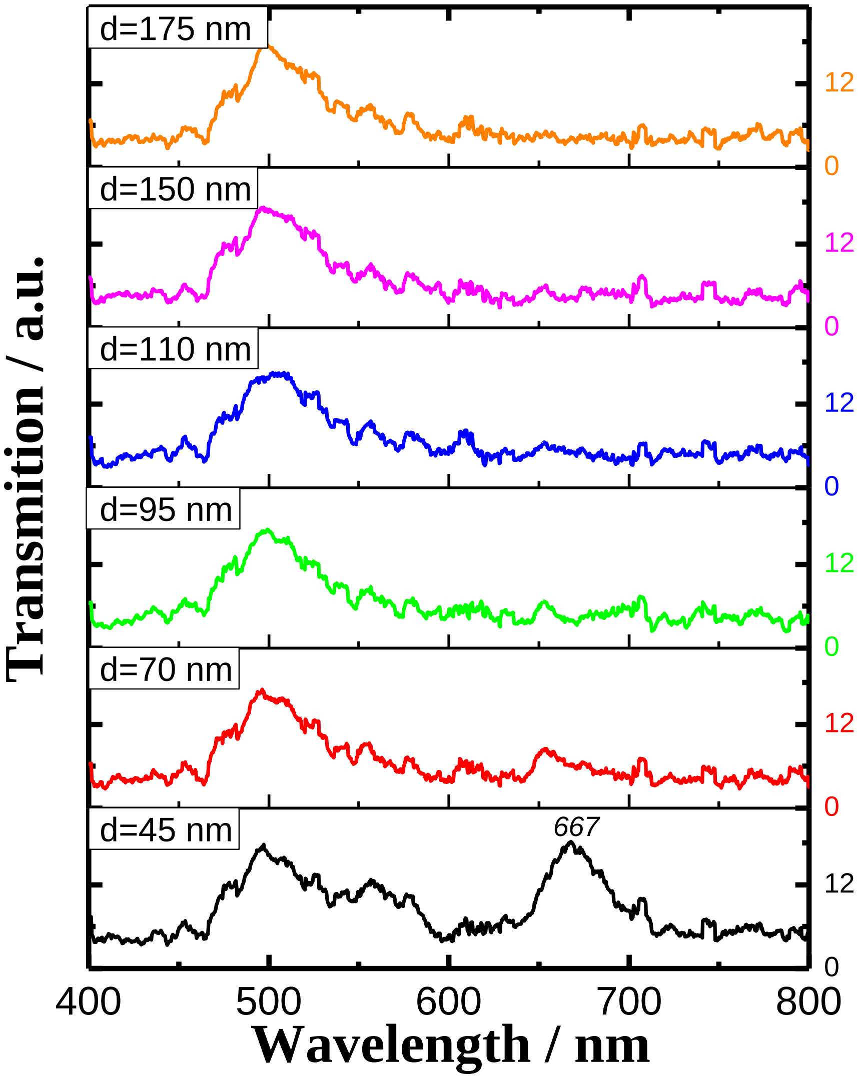

Figure 3.13 White light transmission spectra of cross bow-tie nano-aperture arrays with different tip-to-tip distances. As descripted in Section 2.1, Chapter 2, all these nano-apertures were drilled in gold films of 100 nm thickness. The base of the triangle was 120 nm and the corresponding height was 120 nm. The periodicities for all the arrays were the same, 600 nm. The tip-to-tip distances of the facing triangles were 45 nm, 70 nm, 95 nm, 110 nm, 150 nm and 175 nm respectively. The interband sp-d transition peak at 490 nm was un-removed in all these spectra.

Figure 3.13 shows the white light transmission spectra where the cross bow-tie nano-aperture arrays were used to achieve SPR. Six different types of cross bow-tie nano-aperture arrays were characterized. As given in Section 2.1, Chapter 2, all these cross bow-tie nano-aperture arrays shared the same periodicity, but with varied in the tip-to-tip distances. In contrast to the white light transmission circular and bow-tie nano-aperture arrays, the spectra in Figure 3.13 were plotted as transmission instead of transmittance (i.e. they are the raw data with no further background correction). Due to the low signal/noise in the raw transmission data, the removal of the interband sp-d transition from the gold film and dark noise would result in a spectrum completely swamped by noise.

Only one peak at 667 nm for the tip-to-tip distance of 45 nm can possibly be attributed to SPR. There are several other peaks observed in these spectra as well. The gold layer’s interband sp-d transition peak at 490 nm was presented in all spectra. The lack of characteristic SPR enhanced transmission peaks from the top five spectra in Figure 3.13, which corresponds to cross bow-tie nano-aperture arrays with tip-to-tip distances ranging from 70 nm to 175 nm, indicates that those arrays were not drilled completely through the gold layer to reach the glass. In this case, the incident light was blocked by the residue metal layer.

Fabrication experiments showed that the shape of the cross bow-tie aperture could not be maintained if the milling time in the FIB was increased to allow the total removal of the metal layer. More fabrication tests are required to produce cross bow-tie nano-aperture arrays milled completely through the gold film.

Reference:

[1] Thio T, Ghaemi HF, Lezec HJ, Wolff PA, Ebbesen TW **1999** Surface-plasmon-enhanced Transmission through Hole Arrays in Cr Films *J. Opt. Soc. Am. B* 16, 1743-1748

[2] Ebbesen T W, Lezec HJ, Ghaemi HF, Thio T, Wolff PA **1998** Extraordinary Optical Transmission Through Sub-wavelength Hole Arrays *Nature* 391, 667-669

[3] Gao H, Henzie J, Odom TW **2006** Direct Evidence for Surface Plasmon-Mediated Enhanced Light Transmission through Metallic Nanohole Arrays *Nano Lett.* 6, 2104-2018

[4] Lamprecht B, Krenn JR, Schider G, Ditlbacher H, Salerno M, Felidj N, Leitner A, Aussenegg FR **2001** Surface Plasmon Propagation in Microscale Metal Stripes *Appl. Phys. Lett.* 79, 51-53

[5] Shulz LG **1954** The Optical Constants of Silver, Gold, Copper, and Aluminum. I. The Absorption Coefficient k *J. Opt. Soc. Am.* 44, 357-362

[6] Ordal MA, Long LL, Bell RJ, Bell SE, Alexander RW Jr., Ward CA **1983** Optical Properties of the Metals Al, Co, Cu, Au, Fe, Pb, Ni, Pd, Pt, Ag, Ti, and W in the Infrared and Far Infrared *Appl. Opt.* 22, 1099-1119

[7] Genet C, van Exter MP, Woerdman JP **2003** Fano-type Interpretation of Red Shifts and Red Tails in Hole Array Transmission Spectra *Optics Communications* 225, 331-336

[8] Liu Y, Blair S **2003** Fluorescence Enhancement from an Array of Subwavelength Metal Apertures *Opt. Lett.* 28, 507-509

[9] Brolo AG, Arctander E, Gordon R, Leathem B, Kavanah KL **2004** Nanohole-Enhanced Raman Scattering *Nano Lett*. 4, 2015-2018

[10] Stiles P, Dieringer J, Shah NC, Van Duyne RP **2008** Surface-Enhanced Raman Spectroscopy *Ann. Rev. Anal. Chem.* 1, 601-626

[11] Lesuffleur A, Kumar LKS, Brolo AG, Kavanagh KL, Gordon R **2007** Apex-enhanced Raman Spectroscopy using Double-hole Arrays in a Gold Film *J. Phys. Chem. C* 111, 2347-2350

[12] Yang Z, Li Q, Ren B, Tian Z **2011** Tunable SERS from Aluminium Nanohole Arrays in the Ultraviolet Region *Chem. Comm.* 47, 3909-3911

[13] Gordon R, Hughes M, Leathem B, Kavanagh KL, Brolo AG **2005** Basis and Lattice Polarization Mechanisms for Light Transmission through Nanohole Arrays in Metal Films *Nano Lett.* 5, 1243-1246

[14] Le Ru EC, Galloway C, Etchegoin PG **2006** On the Connection between Optical Absorption/Extinction and SERS Enhancements *Phys. Chem. Chem. Phys*. 8, 3083-3087

[15] Prucha EJ, Ghosh G **1998** Handbook of Optical Constants of Solids *Academic Press*

Chapter 4: Surface Enhanced Raman Scattering (SERS) from Nano-aperture Arrays

In this chapter, the surface enhanced Raman scattering (SERS) properties of different nano-aperture arrays will be presented. The experiments were realized using a Renishaw invia Raman microscope equipped with 632.8 nm laser (detailed description of the experimental setup is given in Chapter 2). The spectra were then treated by Origin to get their baselines removed. The height of the selected Raman peak was used to represent its SERS intensity.

SERS results from nano-aperture arrays under electrochemical conditions will also be presented. The impact of applied electrochemical potential on the SERS intensity was studied to determine the relationship between electrostatic characteristics of the surface and SERS intensity.

Finally, a time series SERS trial from R6G will be presented. Thousands of SERS spectra were taken consecutively from the same sample with the Renishaw system. The data was preceded with PCA and the result will be interpreted.

4.1 SERS Results from Arrays of Circular Nano-apertures

Figure 4.1 shows the SERS spectra of 100 μM R6G from several arrays of circular nano-apertures in gold film with same aperture size but different periodicities. The spectrum at the bottom (Figure 4.1-a) was taken from an un-patterned gold slide. All the spectra were taken under the 632.8 nm excitation (a detailed description of the experimental setup can be found in Section 2.3, Chapter 2). In general, all the arrays enhanced the Raman scattering relative to the un-patterned gold slide. But the magnitude of the SERS enhancement varied with the periodicity.

Five major vibrational bands can be observed from Figure 4.1. According to a calculation using time-dependent density functional theory [1], the band at 1359 cm^{-1} is due to the in-plane C-H bending and the xanthene ring stretch; the band at 1507 cm^{-1} is related to the xanthene ring stretch, C-N stretch, C-H bending and N-H bending; the band at 1573 cm^{-1} is for the xanthene ring stretch, in-plane N-H bending; and the band at 1649 cm^{-1} belongs to the xanthene ring stretch and in-plane C-H bending. Although the band at 1598 cm^{-1}cannot be assigned to one specific vibrational mode, it is commonly found in most R6G SERS spectra [2, 3] and calculation results [4].

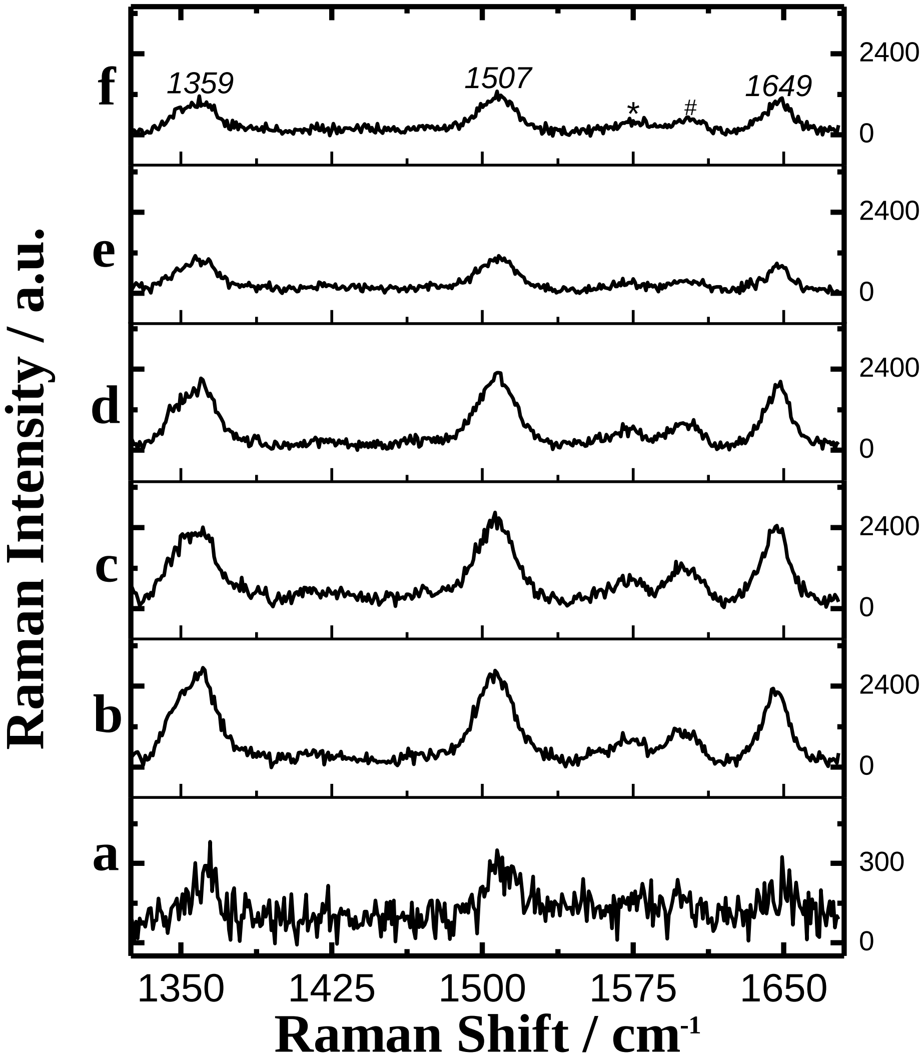

Figure 4.1 SERS spectra from (a) un-patterned gold slide and circular nano-aperture arrays with periodicities of (b) 420 nm, (c) 450 nm, (d) 500 nm, (e) 550 nm, and (f) 600 nm. The diameters of the nano-holes were about 200 nm. The incident laser was 632.8 nm. The concentration of the analyte R6G was 100 μM. Three major peaks at 1359 cm^{-1}, 1507 cm^{-1}, and 1649 cm^{-1}, were labeled in one spectrum. Two other peaks at *1573 cm^{-1}and $^{\#}$1598 cm^{-1}can also be observed. The Raman intensities were adjusted for comparison.

Table 4.1 SERS peak intensity at 1507 cm^{-1} from circular nano-aperture arrays.

Periodicity/ nm	**Au Slide**	**420**	**450**	**500**	**550**	**600**
Intensity/ a.u.	347	2849	2785	2266	1108	1320
Fill Factor/ %	n/a	20.5	15.3	10.5	9.3	8.4
Enhancement Factor	1.0	8.21	8.03	6.53	3.19	3.80
Normalized EF	1.0	8.21	10.8	12.7	7.04	9.28
Transmission Maximum/ nm	n/a	547	569	583	614	651

Table 4.1 shows the Raman peak intensities from the gold slide and different circular nano-aperture arrays. The Raman peak intensity at 1507 cm^{-1} was used as standard [5]. The ratio between the intensities from the circular nano-aperture array and from the gold slide is defined as the SERS enhancement factor. The transmission maxima from all these circular nano-aperture arrays are also given to compare their closeness to the Raman excitation wavelength 632.8 nm. It can be found that arrays with periodicities of 550 nm and 600 nm support SPR peaks closest to the excitation laser. However, better SERS enhancements come from arrays with smaller periodicities (420 nm and 450 nm), whose excited SPR peaks are far from the excitation wavelength.

Past SERS work on circular nano-aperture arrays made from Au (Oxazine 720 used as analyte molecule) [6], Ag [7], Cu [8] and Al [9], all showed that the periodicity of the aperture array would have an impact on the SERS intensity.

Although no straightforward relationship could be drawn based on the periodicity, SPR and SERS enhancement are correlated. It was shown by Equation 3.1 in Chapter 3 that the SPR wavelengths shift with the periodicity of the array. Circular nano-aperture arrays with periodicity in the range between 560 nm and 620 nm support SPR in a wavelength range that covers the excitation laser used in this work (632.8 nm). Our group's previous work [6] showed that the match between the SPR and the excitation laser is a dominant factor driving the SERS enhancement. In another word, higher SERS enhancement is expected when the circular nano-aperture array supports a SPR peak around 632.8 nm. The situation would change when the periodicities of the circular nano-aperture array decreases to about 400 nm to 500 nm. It should be noticed, however, from Figure 3.1, Chapter 2, that the arrays with smaller periodicities presented larger overall transmission and wider SPR peaks due to their relatively large fill factors. SPR excited from circular nano-aperture arrays with periodicities in the 400 nm to 500 nm range has peak wavelengths that are far from 632.8 nm. Nevertheless, the wide transmission peak for those arrays, shown in Figure 3.1 (p=420 nm and p=450 nm) of Chapter 3, allows some overlap between the transmission and the 632.8 nm excitation. The amplitude of the SPR around 632.8 nm supported by the circular nano-aperture arrays with smaller periodicities is in fact stronger than that supported by the other arrays with larger periodicities, even though their intensities have been normalized by the fill factor (see Figure 3.7, Chapter 3). In fact, the circular nano-aperture arrays (p=420 nm and p=450 nm) show the best SERS enhancement in Table 4.1. Therefore, it seems that the amplitude of the transmission at the excitation, rather than the position of the SPR, is the best parameter to estimate the optimum enhancement.

Equation 1.13 in Chapter 1 shows a direct relationship between the SERS enhancement factor and the local electric field at the wavelength of the excitation laser. The local field intensity at 632.8 nm was simulated for all arrays of circular nano-apertures using the FDTD method.

Figure 4.2 shows the comparison between the simulated local field at 632.8 nm and the experimental SERS enhancement factor. The local field on the circular nano-aperture array was simulated in three space directions: E_x, E_y, and E_z, but only the Z direction (perpendicular to the surface) is relevant for SERS. Therefore, the fourth power of the electric field in the Z direction was plotted against the periodicity in Figure 4.2 to predict the SERS enhancement. A good agreement between $|E_z|^4$ and the enhancement factor is readily observed in Figure 4.2. Circular nano-aperture arrays with larger periodicities (550 nm and 600 nm) show weak local field even though the excited SPR from them is around 632.8, the excitation wavelength. These results illustrate that the coincidence between the SPR peak and the excitation laser is not sufficient to predict the SERS enhancement. Since the aperture size was kept constant for all the arrays, a smaller periodicity will result in a larger fill factor. The larger amount of holes allows more light to be transmitted through the smaller periodicities array. In fact, the amount of transmitted light at 633 nm is larger for the 420 nm periodicity array than for the 550 nm array, even considering that the SPR peak of the 550 nm array is closer to 633 nm. This supports the result that these arrays (smaller periodicities) provide stronger local field intensity and SERS enhancement.

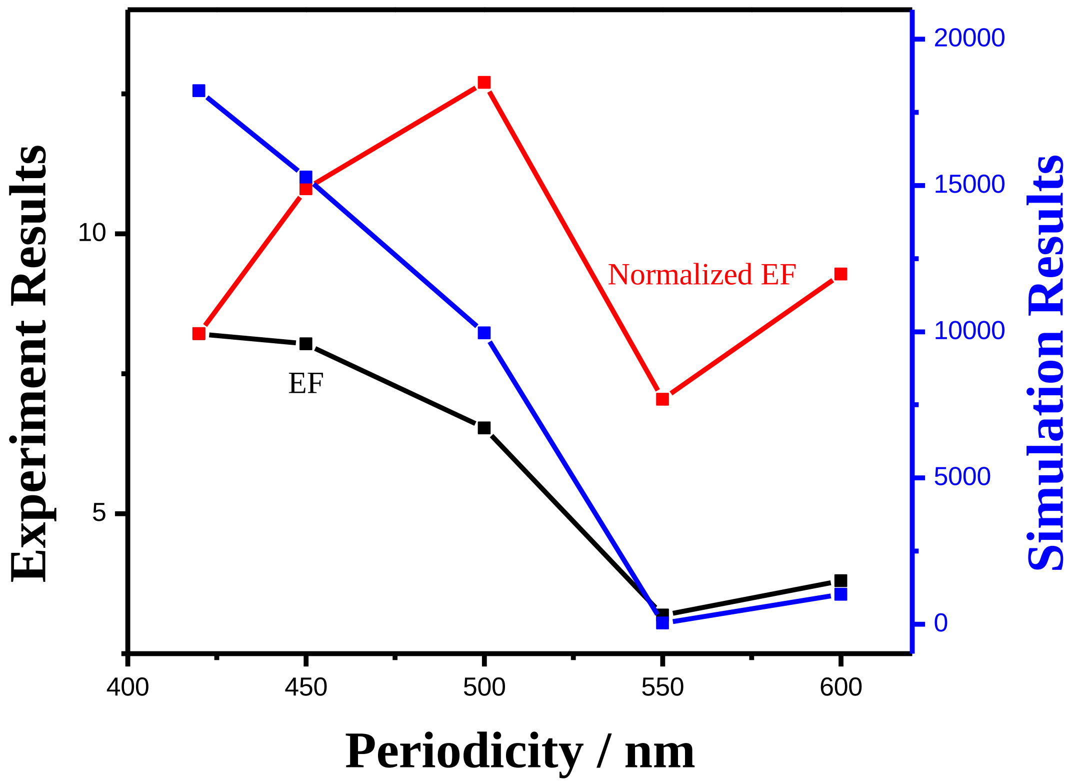

Figure 4.2 The comparison between the simulated electric field, in the form of $|E_z|^4$, and the experimental enhancement factors. The data in red is the EF normalized with the fill factor.

Previous work [7] showed that roughness in the metal layer (Ag for its case) generated by the fabrication might create “hot spot” that contribute to increase the SERS enhancement. Although circular nano-aperture arrays with smaller periodicities possess more roughness, the increase in roughness should not be the main reason for their better SERS enhancement. The FDTD simulation in Figure 4.2 suffers no impact from the roughness of thin gold layer, while it shows that the local fields at the smaller periodicity arrays are expected to have stronger intensities.

4.2 SERS Results from Arrays of Bow-tie Nano-apertures

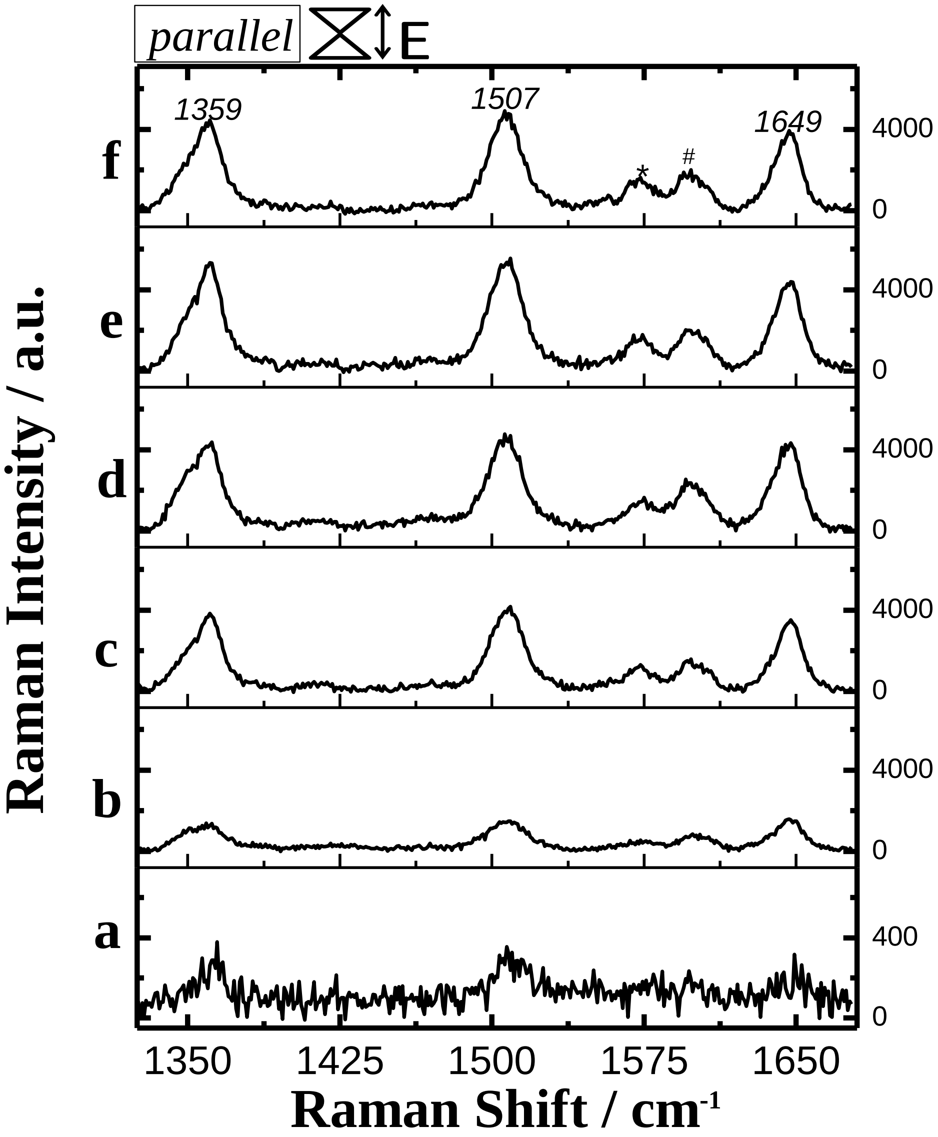

Figure 4.3 SERS spectra from (a) un-patterned gold slide and bow-tie nano-aperture arrays with different tip-to-tip distances of (b) -50 nm (overlapped), (c) 0 nm, (d) 50 nm, (e) 75 nm, and (f) 110 nm respectively. The incident laser was 632.8 nm and polarized parallel to the bow-tie aperture. The concentration of the analyte R6G was 100 μM. Three major peaks at 1359 cm^{-1}, 1507 cm^{-1}, and 1649 cm^{-1}, were labeled in one spectrum. Two peaks at *1573 $cm^{-1}$and $^{\#}$1598 cm^{-1} can also be observed from the spectra. The Raman intensities scales were adjusted for comparison.

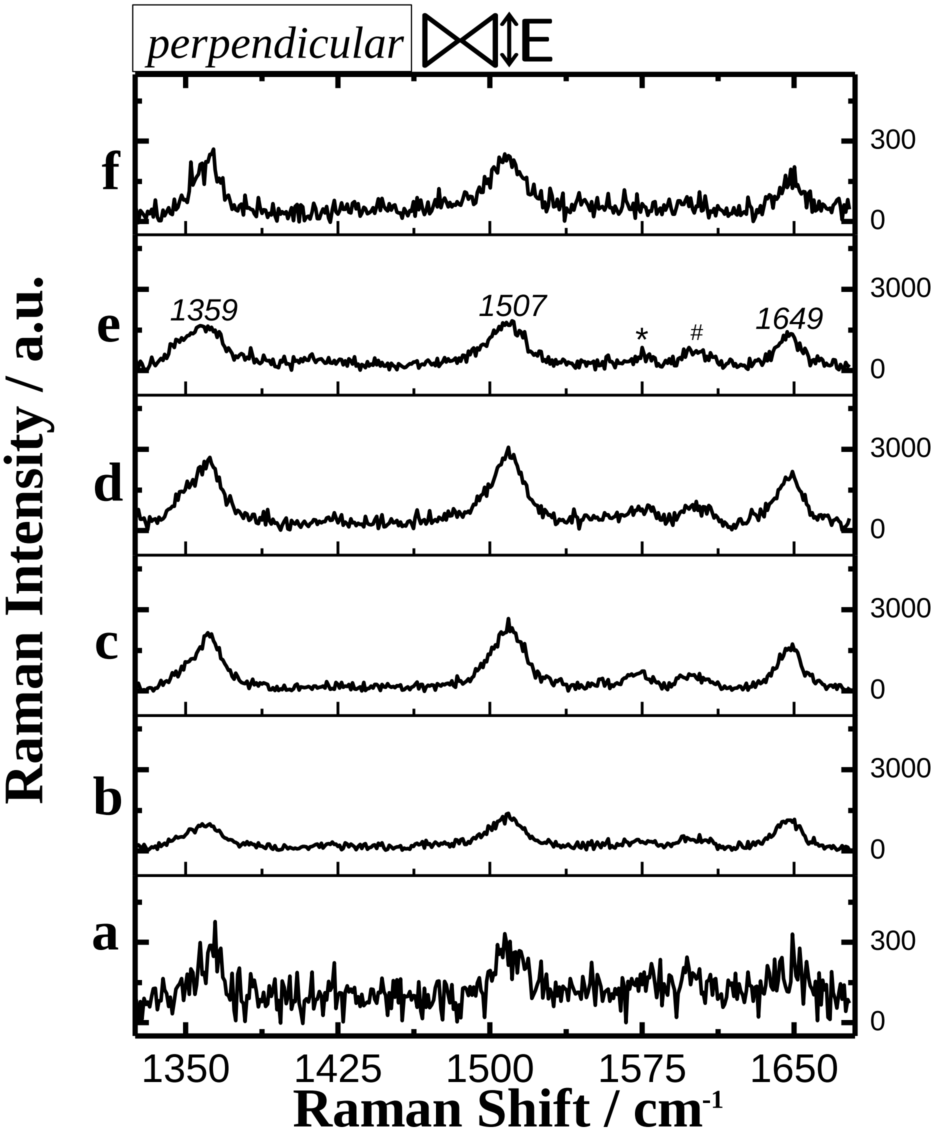

Figure 4.4 SERS spectra from (a) un-patterned gold slide and bow-tie nano-aperture arrays with different tip-to-tip distances of (b) -50 nm (overlapped), (c) 0 nm, (d) 50 nm, (e) 75 nm, and (f) 110 nm respectively. The incident laser was 632.8 nm and polarized perpendicular to the bow-tie aperture. The concentration of the analyte R6G was 100 μM. Three major peaks at 1359 cm^{-1}, 1507 cm^{-1}, and 1649 cm^{-1}, were labeled in one spectrum. Two other peaks at *1573 cm^{-1}and $^{\#}$1598 cm^{-1}can also be observed. The Raman intensities scales were adjusted for comparison.

Figure 4.3 and Figure 4.4 show the SERS spectra of 100 μM R6G from several arrays of bow-tie nano-apertures and from a reference, un-patterned, gold slide surface. Both figures present SERS spectra taken under the 632.8 nm excitation laser, but polarized parallel to the bow-tie aperture for Figure 4.3 and perpendicular for Figure 4.4 (as shown by the schemes in both figures). As discussed in Chapter 2, all the bow-tie nano-aperture arrays have the same 600 nm periodicity and aperture size (except the overlapped aperture), but their tip-to-tip distances change from -50 nm (overlapped) to 110 nm. In general, all the arrays enhance the Raman scattering. But the enhancement property varies with the tip-to-tip distance and the direction of the polarized laser to the aperture axis.

Five Raman bands, at 1359 cm^{-1}, 1507 cm^{-1}, *1573 cm^{-1}, $^{\#}$1598 cm^{-1}and 1649 cm^{-1}, can be observed in both Figure 4.3 and Figure 4.4. They are the same as observed from the circular nano-aperture arrays.

Table 4.2 SERS peak intensity at 1507 cm^{-1} from bow-tie nano-aperture arrays.

$D_{\text{tip-to-tip}}$/ nm	**Au Slide**	**-50**	**0**	**50**	**75**	**110**
Fill Factor / %	N/A	12.3	11.6	10.4	10.9	10.5
I_{Parallel}/ a.u.	347	1480	4176	4738	5476	5004
EF_{Parallel}	1.0	4.3	12.0	13.7	15.8	14.4
***Normalized* EF_{Parallel}**	N/A	4.3	12.7	16.2	17.8	16.9
$P_{\text{Perpendicular}}$ / a.u.	347	1356	2668	3012	1808	250
$EF_{\text{Perpendicular}}$	1.0	3.9	7.7	8.7	5.2	0.7
***Normalized* $EF_{\text{Perpendicular}}$**	N/A	3.9	8.2	10.3	5.9	0.8
$\frac{EF_{Parallel}}{EF_{Perpendicular}}$	1.0	1.1	1.6	1.6	3.0	20.0
Transmission Maximum /nm	N/A	656	646	636	627	618

D stands for Distance, *I* stands for Intensity, and *EF* stands for Enhancement Factor.

Table 4.2 shows the Raman peak intensities from the gold slide and different bow-tie nano-aperture arrays. As preceded with the same method used in Table 4.1, the enhancement factors for both the parallel and perpendicular directions are calculated and compared. The transmission maxima from these arrays are also given to indicate their closeness to the excitation wavelength 632.8 nm. For the parallel polarization situation, a good agreement between the trend in SERS enhancement factors and the position of the SPR peak can be found in Table 4.2. The bow-tie nano-aperture arrays with tip-to-tip distances between 50 nm and 110 nm correlate with the best SERS enhancement, while these arrays support SPR peak around 632.8 nm. For the perpendicular polarization situation, the magnitude of the SERS enhancement is not as strong as for the parallel polarization. The overlapped aperture (-50 nm), on the other hand, presented relatively small difference in the SERS intensity from both polarizations, showing a smaller degree of structural anisotropy. The same sort of matching between the SPR wavelength and SERS enhancement was also observed for the experiments using perpendicular polarization. It is important to note the abnormally small SERS intensity for the bow-tie nano-aperture array with 110 nm tip-to-tip distance.

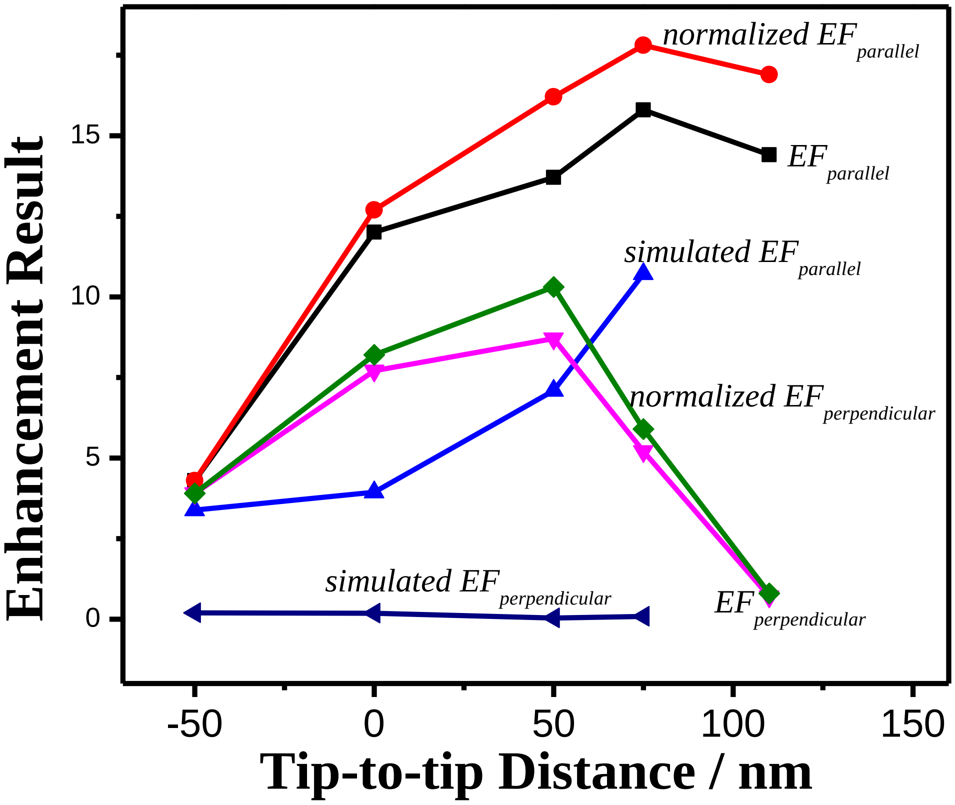

Figure 4.5 The comparison between the simulated electric field, in the form of $|E_{632.8}|^2 * |E_{701}|^2$, and the experimental enhancement factor.

Figure 4.5 shows the comparison between the simulated field intensity (relative to unic cell) and the experimental SERS enhancement factor. The simulated electric filed was presented by the product of the square of the field intensity at 632.8 nm and the square of the field intensity at 701 nm, the same as the Raman peak at 1507 cm^{-1}.

In contrast to the circular nano-aperture arrays, all the bow-tie nano-aperture arrays share the same periodicity and aperture size (the only exception is the overlapped). This resulted in similar values of fill factors (see Table 3.7 in Chapter 3). It can also be found in Figure 3.8 of Chapter 3, that all the five bow-tie nano-aperture arrays have similar peak transmittance intensity and similar peak width. These similarities simplify the relationship between the SERS enhancement and the geometrical parameters of the bow-tie apertures. Tip-to-tip distance, as the only varying parameter, determines the SPR wavelength supported by the bow-tie nano-aperture array. As shown in Table 4.2, the increased tip-to-tip distance will lead one of the transmission maxima to shift to lower wavelength. Bow-tie nano-aperture arrays with tip-to-tip distances from 50 nm to 110 nm support SPR peak closest to the excitation laser. Under similar SPR peak intensity and width, the SPR peak approximation correlates well with the SERS enhancement. The best SERS was observed from bow-tie nano-aperture arrays with SPR close 632.8 nm. The SERS enhancement decreased when the excited SPR wavelength was removed from the laser excitation.Another difference between circular and bow-tie nano-aperture is their anisotropy. The bow-tie nano-aperture is not symmetric in all directions. As the excitation laser is polarized, the direction of polarization relative to the bow-tie nano-aperture has an impact in the SPR, and then in the SERS enhancement. Although no polarized white light transmission spectrum has been measured in this work, theoretical simulation showed that the direction between the polarization and the bow-tie aperture axis should lead to different transmission results [10]. Previous work on bow-tie nano-aperture [11] showed that stronger excitation was observed when the laser is polarized parallel to the bow-tie axis. This is also the result shown in Table 4.2. The average EF_{Parallel} is larger than the average $EF_{\text{Perpendicular}}$ for all arrays, except for the overlapped bow-tie nano-aperture (see Figure 2.3 in Chapter 2). The EFs (for both parallel and perpendicular polarization situations) from the bow-tie nano-aperture array with -50 nm tip-to-tip distance were close to that observed from the circular nano-aperture array with same periodicity (600 nm). The slight larger EF (4.3/3.9 to 3.8) can be justified by the roughness caused by the wedge shape of the bow-tie aperture.

4.3 SERS Results from Arrays of Cross Bow-tie Nano-apertures

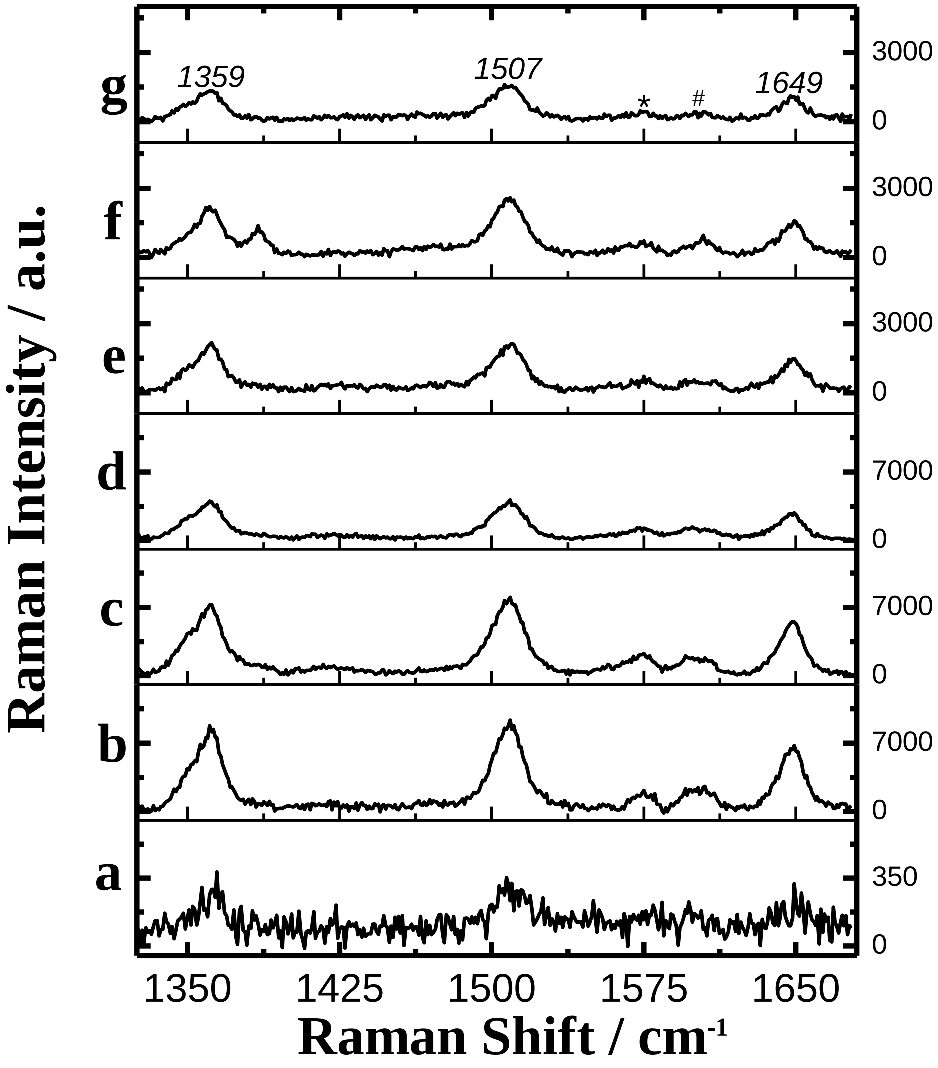

Figure 4.6 SERS spectra from (a) un-patterned gold slide and cross bow-tie nano-aperture arrays with different tip-to-tip distances of (b) 45 nm, (c) 70 nm, (d) 95 nm, (e) 110 nm, (f) 150 nm and (g) 175 nm respectively. The incident laser was 632.8 nm. The concentration of the analyte R6G was 100 μM. Three major peaks at 1359 cm^{-1},

1507 cm^{-1}, and 1649 cm^{-1}, were labeled in one spectrum. Two other peaks at *1573 $cm^{-1}$and #1598 cm^{-1}can also be observed. The Raman intensities scales were adjusted for comparison.

Figure 4.6 shows the SERS spectra of 100 μM R6G from several arrays of cross bow-tie nano-apertures and from a reference. All the spectra were taken under the 632.8 nm excitation. As discussed in Chapter 2, all the cross bow-tie nano-aperture arrays have the same 600 nm periodicity and aperture size, but their tip-to-tip distances change from 45 nm to 175 nm. Five Raman bands, at 1359 cm^{-1}, 1507 cm^{-1}, *1573 cm^{-1}, #1598 $cm^{-1}$and 1649 cm^{-1} can be observed from all the spectra. The intensities of all the Raman bands show that the cross bow-tie nano-aperture arrays will enhance the Raman scattering in general. However, the variations of the tip-to-tip distance have an impact on the enhancement property.

Table 4.3 SERS peak intensity at 1507 cm^{-1} from cross bow-tie nano-aperture arrays.

$D_{\text{tip-to-tip}}$/ nm	Au Slide	45	70	95	110	150	175
Fill Factor / %	N/A	7.7	6.7	8.3	8.3	7.7	8.6
Intensity/ a.u.	347	9261	7932	4073	2114	2554	1580
Enhancement Factor	1.0	26.7	22.9	11.7	6.09	7.36	4.55
Normalized EF	N/A	26.7	26.3	10.9	5.6	7.4	4.1

Table 4.3 shows the Raman peak intensity at 1507 cm^{-1} from cross bow-tie nano-aperture arrays with tip-to-tip distance from 45 nm to 175 nm. Better SERS enhancements can be observed from cross bow-tie nano-aperture arrays with tip-to-tip distance from 45 nm to 95 nm. The SERS intensity decreases as the tip-to-tip distance increase.

The white light transmission data shown in Figure 3.13 of Chapter 3 indicates that cross bow-tie nano-apertures with larger tip-to-tip distance might not have been drilled completely though the metal film. However, this should not affect these arrays' ability to support SPR. Other works [14, 18] show that the excitation SPR does not require complete milling through the apertures but periodical patterning at the gold surface in the appropriated length scale. Table 4.2 shows that, for bow-tie nano-aperture arrays, the SERS EF increases with the tip-to-tip distance, maximizes for separation between 50 nm and 100 nm, and decreases for larger tip-to-tip distances. The same trend has been observed in Table 4.3 for cross bow-tie nano-aperture arrays. In that case, the SERS EF increased with the tip-to-tip distance (up to 95 nm) separation and then decreased as the tip-to-tip distance increased.

It is suggested that bow-tie nano-apertures focusers capable of focusing the local field to the gap between their two triangular apertures [12]. With this idea, the cross bow-tie nano-aperture is designed and supposed to focus the local fields even better. Both simulation result in Figure 4.2 and the small EF difference (4.3/3.9 to 3.8) from the bow-tie and circular aperture arrays prove that increased roughness in thin gold layer is not a main factor to the SERS enhancement properties of the nano-aperture arrays. Therefore, the increased roughness in cross bow-tie nano-aperture arrays should not correlate with their large EF values. On the other hand, the decreased fill factor would result in a weaker SPR and therefore a weaker SERS enhancement property (as discussed in Section 4.1). This is not the case observed in the cross bow-tie nano-aperture arrays. Each cross bow-tie aperture has four triangular apertures with about 120 nm base and 120 nm height, equal to 28,800 nm^2 area. However, the bow-tie nano-aperture has an average of 40, 000 nm^2 area. The great SERS enhancement shown in Table 4.3 should indicate the improved field localization ability of the cross bow-tie nano-aperture array.

4.4 Comparison of SERS from Arrays of Different Nano-apertures

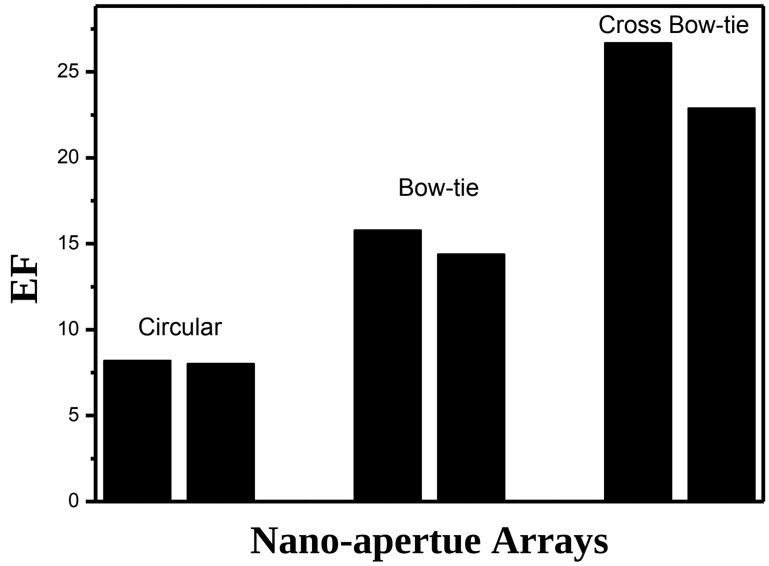

Figure 4.7 Comparison of SERS enhancement factors from circular (420 nm and 450 nm periodicities), bow-tie (75 nm and 110 nm tip-to-tip distances) and cross bow-tie (45 nm and 70 nm tip-to-tip distances) nano-aperture arrays.

Figure 4.7 shows the comparison of SERS EF from all the different kinds of nano-aperture arrays studied in this work. The two nano-aperture arrays from each hole-shape (circular, bow-tie, and cross bow-tie) chosen for this comparison are the ones with stronger SERS EF. In the case of bow-tie nano-aperture, the data in Figure 4.6 is for laser excitation polarized parallel to the bow-tie basis. Figure 4.7 clearly shows that bow-tie and cross bow-tie nano-aperture arrays present better SERS EF.

4.5 SERS from Nano-aperture Array under Electrochemical Condition

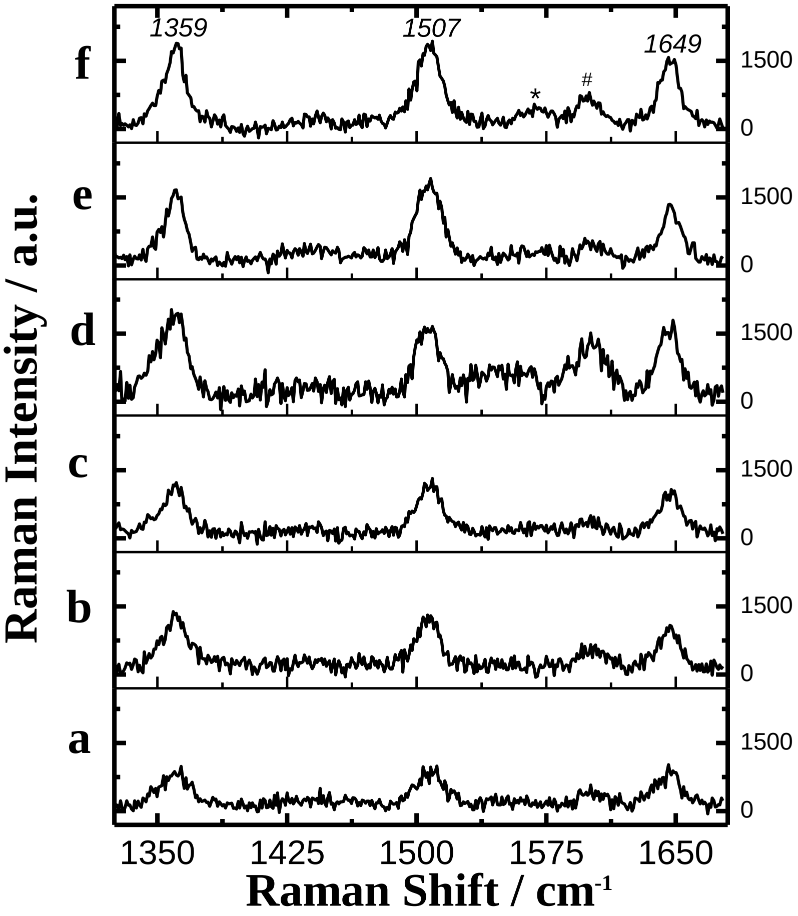

Figure 4.8 SERS spectra from a bow-tie nano-aperture array with tip-to-tip distance of 75 nm under electrochemical potentials (vs Ag/AgCl reference electrode) of (a) 200 mV, (b) 100 mV, (c) 0 mV, (d) -100 mV, (e) -200 mV, and (f) -300 mV. The incident laser was 632.8 nm and its polarization is in the parallel direction relative to the aperture. The analyte was 25 μM R6G in 0.1 M $KClO_4$ solution.

Figure 4.8 shows the SERS spectra of 25 μM R6G in 0.1 M $KClO_4$ solution under a series of electrochemical potentials. All these spectra were taken sequentially and “in situ” from the same bow-tie nano-aperture (tip-to-tip distance of 75 nm). The incident laser wavelength was 632.8 nm and its electric field polarization was set in parallel relative to the bow-tie nano-aperture (defined in Figure 4.3). The SERS signal decreased as the applied electrochemical potential became more positive (from (a) +200 mV to (f) -300 mV), as summarized in Figure 4.8.

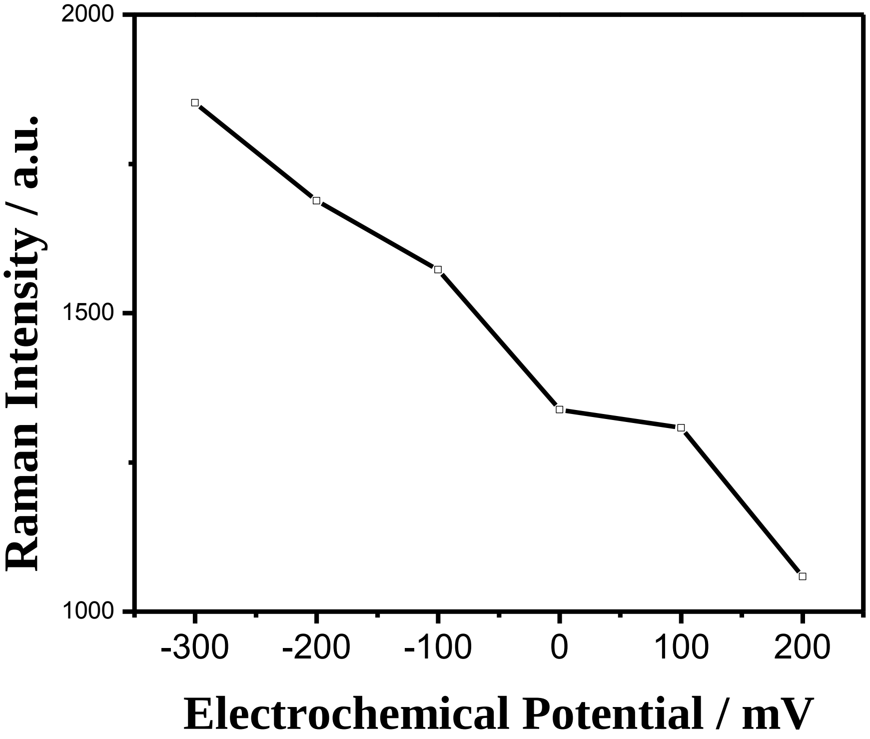

Figure 4.9 SERS intensities of the 1507 cm^{-1} R6G band plotted versus the applied potential. The substrate was a bow-tie nano-aperture with 75 nm tip-to-tip distance. The excitation laser is 632.8 nm and polarized in parallel direction to the aperture. 25 μM R6G in 0.1 M $KClO_4$ solution was used as the analyte sample.

Of the two mechanisms of SERS, the chemical mechanism is generally invoked to explain the dependence of the SERS signal on the applied potential under electrochemical condition [15]. According to the chemical mechanism, the applied electrochemical potential control the position of the Fermi level on the SERS substrates, tuning the electron transfer between the metal and the adsorbed molecule [16]. When the energy of this charge transfer process matches the laser excitation, an additional enhancement, similar to resonance Raman effect, provides an additional contribution to SERS. Another possibility to explain the trend of SERS intensities with applied potential is related to the control of the surface coverage of the adsorbate by the applied potential. For instance, the applied electrochemical potential substrates will change the surface charge, resulting in variations in the electrostatic interaction between the charged substrate surface and the ionic analyte molecules. This interaction can either attractive or repulsive, depending on the applied potential [5]. This simple model fits well with the results presented in Figure 4.8. The cationic R6G molecule is expected to adsorb preferentially when the gold surface is negatively charged (the pzc for Au is 170 mV to Ag/AgCl electode [19]). The larger surface coverage at more negative potentials would increase the probability of a molecule to be at the hot spot [5, 13]. However, contributions from the chemical mechanism, as described above, cannot be completely excluded.

4.6 PCA Application in the Time Series SERS Data

Strong time-dependent fluctuations in SERS intensities have been reported SERS substances immersed in diluted solutions of the analyte [5]. This fluctuation has been assigned to the analyte molecule travelling in and out of high efficient “hot spots” [17]. The SERS signal from these “hot spots” is normally much stronger than the average, resulting in the signal fluctuation affected by diffusion. This phenomenon is widely observed from a series of SERS substrates [14]. To study this phenomenon, a collection of SERS signal over a long period of time is required. This kind of long time exposure to the laser can cause degradation to the sample. The SERS features of the degradation products must be identified and eliminated from the statistical analysis. Another problem of this study is the low signal-to-noise ratio resulted from the low analyte concentration.

PCA treatment of the time series SERS data can differentiate the degraded SERS signal and increase the signal-to-noise ratio [5]. Time series SERS data was collected from 100 μM R6G on a circular nano-aperture array (420 nm periodicity) to be used as an example for the PCA application.

Detailed experimental procedures can be found in Chapter 2.

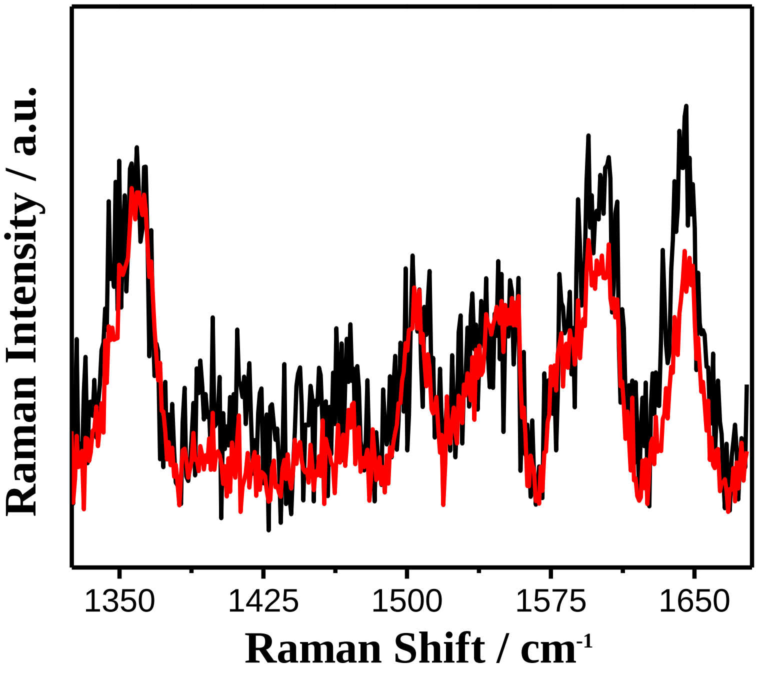

Figure 4.10 Comparison of a time series SERS spectrum (the black one) with its PCA preceded spectrum (the red one).

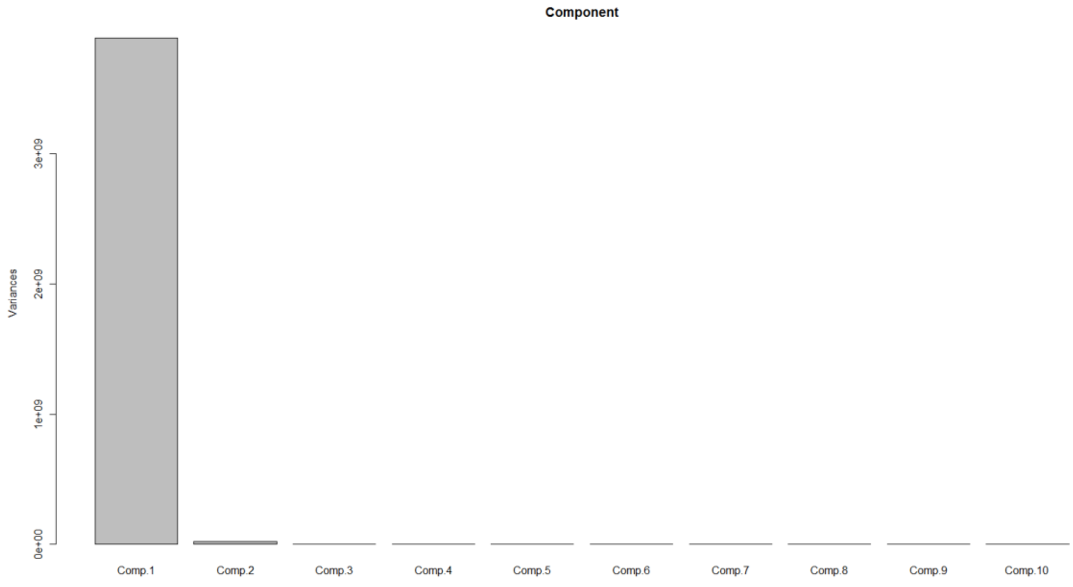

Figure 4.11 Primary components used to represent time series SERS intensity.

Three thousand of SERS spectra were taken from the same sample one after the other in a time series. Statistical analysis using PCA procedure of all these three thousand sets of SERS intensity data would decompose each set of data and then represent it with specific coefficient and a common set of components.

Figure 4.10 shows the original SERS spectra of 100 µM R6G from a circular nano-aperture array (420 nm periodicity) and its PCA treated spectrum. Obvious increase in the signal-to-noise ratio can be read from this comparison.

Figure 4.11 shows the variance of the primary component. The bigger the variance is, the more importantly it serves to the spectrum. It can found that only the first two components are important to represent the character of the Raman bands, while all the other components are just minor characteristic variances that represent mainly the noise fluctuations. Therefore, the noise in a SERS spectrum could be reduced if this spectrum gets represented by only the first two components. This result can be found in Figure 4.10, the red (represented by the first two components) spectrum shows much less noise.

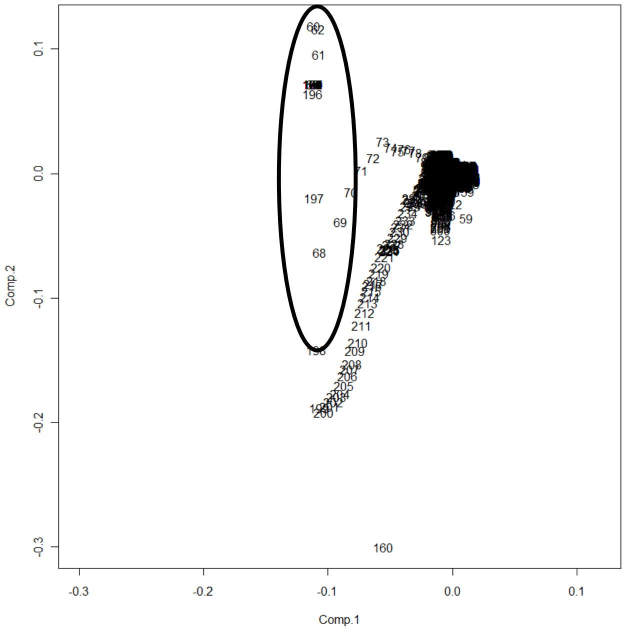

Figure 4.12 Bi-plot of the first two components from the PCA treated SERS intensity data. The number in this plot represents a set of SERS intensity data.

Figure 4.12 shows the plot of each SERS intensity data's first component against its second component. The number in this plot represents which set of SERS intensity data is plotted. It can be found in this plot that most SERS intensity data sets' first two components are similar to each other, while there are still a few data sets' components are different from the main group. These data sets are circled in Figure 4.12. They represent the SERS spectrum taken from degraded samples and need to be picked out from the time series study.

Reference:

[1] Jensen L, Schatz GC **2006** Resonance Raman Scattering of R6G as Calculated Using Time-Dependent Density Functional Theory *J. Phys. Chem. A* 110, 5973-5977

[2] Michaels AM, Jiang J, Brus L **2000** Ag Nanocrystal Junctions as the Site for Surface-Enhanced Raman Scattering of Single R6G Molecules *J. Phys. Chem. B* 104, 11965-11971

[3] Hildebrandt P, Stockburger M **1984** Surface-Enhanced Resonance Raman Spectroscopy of R6G Adsorbed on Colloidal Silver *J. Phys. Chem.* 88, 5935-5944

[4] Watanabe H, Hayazawa N, Inouye Y, Kawata S **2005** DFT Vibrational Calculations of R6G Adsorbed on Silver: Analysis of Tip-Enhanced Raman Spectroscopy *J. Phys. Chem. B* 109, 5012-5020

[5] dos Santos DP, Andrade GFS, Temperini MLA, Brolo AG **2009** Electrochemical Control of the Time-dependent Intensity Fluctuations in Surface-enhanced Raman Scattering (SERS) *J. Phys. Chem. C* 113, 17737-17744

[6] Brolo AG, Arctander E, Gordon R, Leathem B, Kavanah KL **2004** Nanohole-Enhanced Raman Scattering *Nano Lett*. 4, 2015-2018

[7] Reilly T, Chang S, Corbman JD, Schatz GC, Rowlen KL **2007** Quantitative Evaluation of Plasmon Enhanced Raman Scattering from Nanoaperture Arrays *J. Phys. Chem. C* 111, 1689-1694

[8] Anema J, Marthandam P, Gordon R, Brolo AG **2008** Enhanced Raman Scattering from Nanoholes in a Copper Film *J. Phys. Chem. C* 112, 17051-17055

[9] Yang Z, Li Q, Ren B, Tian Z **2011** Tunable SERS from Aluminium Nanohole Arrays in the Ultraviolet Region *Chem. Commun*. 47, 3909-3911

[10] Kinzel EC, Xu X **2010** Extraordinary Infrared Transmission Through a Periodic Bowtie Aperture Array *Optics Letters* 35, 992-994

[11] Wang L, Uppuluri SMV, Jin EX, Xu X **2006** Nanolithography using High Transmission Nanoscale Ridge Apertures *Nano Lett*. 6, 361-364

[12] Srisungsitthisunti P, Ersoy OK, Xu X **2011** Improving Near-field Confinement of a Bowtie Aperture using Surface Plasmon Polaritons *Appl. Phys. Lett*. 98, 223106

[13] Bockris JO'M, Shaded UMK **1993** Surface Electrochemistry: a Molecular Level Approach Plenum Press, New York

[14] Andrade GFS, Min Q, Gordon R, Brolo AG **2012** Surface-Enhanced Resonance Raman Scattering on Gold Concentric Rings: Polarization Dependence and Intensity Fluctuations *J. Phys. Chem. C* 116, 2672-2676

[15] Iannelli A, Brolo AG, Irish DE, Lipkowski J **1997** Electrochemical and Raman Spectroscopic Studies of Pyrazine Adsorption at the Au (210) Electrode Surface *Canadian Journal of Chemistry* 75,1694-1702

[16] Cardona M, Guntherodt G **1984** Light Scattering in Solids IV: Electronic Scattering, Spin Effects, SERS and Morphic Effects *Springer-Verlag: Berlin, Germany* 1984, 289-418

[17] Lim DK, Jeon KS, Kim HM, Nam JM, Suh YD **2010** Nanogap-engineerable Raman-active Nanodumbbells for Single-molecule Detection *Nat.Mater.* 9, 60-67

[18] Qiao M, Santos MJL, Girotto EM, Brolo AG, Gordon R **2008** Localized Raman Enhancement from a Double-Hole Nanostructure in a Metal Film *J. Phys. Chem. C* 112, 15098-15101

[19] Bochris, JO'M, Argade, SD, Gileadi, E 1969 The Determination of the Potentials of Zero Charge on Solid Metals *Elcctrochimica Acta* 14, 1259-1283

Chapter 5: Summary

In this work, arrays of circular, bow-tie, and cross bow-tie nano-apertures were fabricated and imaged by SEM. Spectroscopic experiments show that nano-aperture arrays can be used to excite and support SPR. The SPR obtained would couple with incident lights and amplify the local electric field on these arrays, serving them as efficient SERS substrates.

White light spectra show that the shape of the nano-aperture array and each array's parameter variances would affect the array's EOT property. The transmission maxima would shift with the periodicity. And even under the same periodicity, the shape of the nano-aperture would induce transmission peaks with different wavelengths. For the bow-tie nano-aperture arrays, the interaction between two facing triangle apertures is found to have an impact on the transmission maxima. The farther apart these two triangle apertures are, the less they interact and similar transmission peaks can be observed. On the other hand, the fill factor of each array would influence the transmission. Bigger fill factor would result in wider peaks and stronger transmission intensity.

SERS spectra show that the achieved SPR on all the nano-aperture arrays would enhance the Raman scattering. The enhancement ability varies with the aperture shape and its parameter variance. On average, the cross bow-tie nano-aperture arrays show the best SERS enhancement. Simple relation between the white light transmission and SERS result is concluded. Under the situation of similar white light transmission peak width and intensity, the closer the excited SPR peak to the excitation laser is, the better the SERS enhancement result can be found in each type of nano-aperture arrays. When different fill factors are involved, the SERS result is in direct relationship with the local field intensity.

Applied electrochemical potential influenced SERS and PCA application were also studied. PCA method was applied in the time-series SERS data analysis and found to be successful in abnormal spectrum removal and signal-to-noise ratio improvement.